NTNU

Norwegian University of
Science and Technology

Predictive Monitoring of Basic Oxygen Steel Refining

Bent Martin Dyrdal

Master of Science in Industrial Cybernetics
Submission date: June 2018
Supervisor: Morten Hovd, ITK
Co-supervisor: Stein O. Wasbø, Cybernetica

Norwegian University of Science and Technology
Department of Engineering Cybernetics

CYBERNETICA
Model based control systems for the process industry

Address: Cybernetica AS
Leirfossveien 27
N-7038 Trondheim
Norway
Phone.: +47 73 82 28 70
Fax: +47 73 82 28 71

MASTER THESIS 2018

To: Bent Martin Dyrdal

Number of pages: 1
Date: 2018-06-12

Predictive monitoring of basic oxygen steel refining

In order to offer their clients tailored products, steel producers are dependent on being able to refine the metal to a wanted quality. This refining takes place in batch processes, usually through several steps. In this thesis there should be made an improved mathematical model of a Basic Oxygen Furnace (BOF), which is a primary steel refining process. This is the first refining step of molten iron with a carbon level at 4-5% to steel with a carbon level typically below 0.5%. The model should be validated with process data from SSAB in Raahe, Finland. In addition, the implementation of a Moving Horizon Estimator (MHE) and a Nonlinear Model Predictive Control (NMPC) should be investigated.

The project will be done in cooperation with Cybernetica AS and SSAB Europe OY.

Work objectives:

- Implement a model for steel refining in Cybernetica's tools.
- Demonstrate that the model can reproduce industrial behaviour.
- Develop a system for better understanding and control of the process.

Work tasks:

- Literature study on steel production and refining processes.
- Further develop the model of metal refining based on previous work.
  - Develop a model for the height of the emulsion layer in the BOF.
  - Evaluate different available models for phosphorus equilibrium from literature.
  - Validate the total energy balance, including off gas and water cooling system.
  - The model should handle continuous temperature monitoring between batches.
- Create an MHE estimator for the process.
  - Validate the model using process data from real process.
  - Configure the MHE-estimator for the process with estimation of the parameter for O_2 utilization and possibly other parameters if needed.
  - Use an estimation horizon of a few previous batches with given product quality to improve predictions of the next batch. Use simulated data for estimation.
- Model predictive monitoring:
  - Implement the NMPC interface in CENIT for predictive monitoring.
  - Configure Cybernetica RealSim for demonstration with end-point prediction of metal composition and temperature.
  - Demonstrate batch-wise simulation with continuous monitoring of temperature in reactor lining between batches.

Adjustments in the work tasks listed above may be done during the project.

Abstract

With the late focus on digitalisation and industry 4.0, many industries have significantly evolved. More instrumentation and automation has led to better maintenance planning, more efficient production and increased safety. However, the steel industry has not been a part of this digitalisation. This is mainly due to its hostile environment with extreme temperatures and pressures, making instrumentation difficult. With few measurements available, the production of steel has been based on experience. It is, therefore, preferable to combine the measurements available with a mathematical model to predict the operating conditions and use these predictions along with a controller. In this work, a first-principles model of a basic oxygen converter has been further developed from a preliminary project. The model is validated against process data given by SSAB and process characteristics described in literature. Using this model, the application of moving horizon estimator and nonlinear model predictive control have been investigated. The estimator and controller performance was tested by using a noise corrupted process simulator.

The results from the modelling showed that the model had a good correlation regarding steel and slag content. However, the need for testing the model against batches with more measurements is evident. The model has too low iron oxide content during oxygen blowing, and the fume's temperature profile does not match the measurements from SSAB. By running test cases with more measurements during blowing, there could be indicators as to why the model deviates from these measurements. For the model-based estimation and control, the estimator showed that with only end-point measurements it was able to estimate parameter values with a slowly varying trend, and the controller met the desired set-point. For large variations in oxygen utilisation, the estimator was not able to estimate the correct value and the controller did not achieve the desired end-point carbon content in the steel. By adding more measurements, the estimation, as expected, improved. However, the estimates were not accurate enough to achieve good end-point prediction.

Sammendrag

Det store fokuset på digitalisering og industri 4.0 har gjort at mange industriar har teke store steg innan instrumentering og automatisering. Dette har ført til at dei har forbetra vedlikehaldet, effektivisert produksjonen og auka sikkerheita. Stålindustrien har ikkje vore med på denne digitaliseringa. Dette kjem av ekstreme temperaturar og trykk, noko som gjer instrumentering vanskeleg. Med få målingar tilgjengeleg, har produksjonen av stål blitt utført basert på operatorens erfaringar. Ved å kombinere dei tilgjengelege målingane med ein matematisk modell, kan ein estimere tilstanden i prosessen og bruke desse estimata saman med ein regulator for å betre resultatet. I dette prosjektet er ein matematisk modell av ein BOF-prosess vidareutvikla frå eit tidlegare prosjekt. Modellen er validert mot prosessdata frå SSAB og prosesskarakteristikk som er beskriven i litteratur. Ved å bruke denne modellen er implementeringa av moving horizon estimator og nonlinear model predictive control studert. Estimatoren og regulatoren er testa ved å bruke ein støyutsatt simulator.

Resultata frå modell-evalueringa viste at modellen hadde god korrelasjon mot stål og slag samansetninga, men det er eit behov for å teste modellen mot batcher med fleire målingar. Modellen har for lågt innhald av jernoksid under blåsinga av oksygen og avgasstemperaturen stemmer ikkje med profilen til målingane frå SSAB. Ved å køyre case-studiar med fleire målingar under prosessen, kan ein finne indikatorar på kvifor modellen viker frå desse målingane. For estimeringa med endepunktsmålingar produserte estimatoren gode estimat for sakte varierande trendar, og regulatoren nådde ønska karboninnhald. For store variasjonar i oksygenutnyttinga klarte ikkje estimatoren å produsere gode nok estimat. Dette førte til at det var stor variasjon mellom estimert- og prosessens karboninnhald. Ved å tilføre fleire målingar blei resultata betre, men ikkje presise nok til å oppnå bra endepunktsprediksjon.

Preface

The work on this project started with an internship at Cybernetica AS the summer of 2017, and continued throughout the fall as a project assignment at NTNU. During this, a model was developed and implemented in Cybernetica's Cenit framework, for more details about the preliminary work the reader is referred to Section 1.4.1. During the preliminary work and this thesis, Cybernetica has provided software and source code necessary to simulate, estimate and control the model. This includes the Cenit framework in which the model has been implemented. This framework contains solvers and the interfaces for configuring the simulator, estimator and controller. The applications used are,

- *Modelfit*
- *Cenit*
- *RealSim*

This is further described in Section 5.1. Cybernetica has also provided guidance and support during the modelling and configuration of the control system.

This master thesis was written during the spring of 2018 as a compulsory part of a 2-year study program leading to an M.Sc. in Industrial Cybernetics at the Norwegian University of Science and Technology (NTNU).

I would like to express my gratitude towards my supervisor, Professor Morten Hovd, for all the support. I would like to thank Cybernetica for providing the tools and support necessary to complete this work. A special thanks to my co-supervisor Dr Stein O. Wasbø and Andreas Hammervold at Cybernetica for always being available for questions and guidance. I would also like to thank SSAB and Seppo Ollila for providing data and knowledge about the process.

Finally, I would like to thank Helena for all the love and support.

Bent Martin Dyrdal
June, 2018

Table of Contents

List of Tables

List of Figures

Abbreviations

BOF/BOP/BOS	Basic Oxygen Furnace/Process/Steelmaking
CV	Controlled Variable
EAF	Electric Arc Furnace
EKF	Extended Kalman Filter
KF	Kalman Filter
LD	Linz-Donawitz
LQG	Linear Quadratic Gaussian controller
LQR	Linear Quadratic Regulator
MHE	Moving Horizon Estimator
MPC	Model Predictive Control
MV	Manipulative Variable
NLP	Nonlinear Programming
NMPC	Nonlinear Model Predictive Control
ODE	Ordinary Differential Equation
OPC	Object Linking and Embedding (OLE) for Process Control
QP	Quadratic Programming
SQL	Sturctured Query Language
SQP	Sequential Quadratic Programming

Nomenclature

Control Symbols

Γ Quadratic state cost MHE

$\hat{\Phi}_T$ Approximation of arrival cost MHE

$\hat{x}$ State estimate

$\mathcal{L}(x_k, \lambda_k)$ Lagrangian function

Φ_T Arrival cost MHE

Π State weighting MHE

θ_k Model parameter vector at time t_k

$f()$ Model function

$g()$ Measurement function

$h()$ Output function

$J()$ Objective function MPC

l_k Stage cost MHE

p SQP search direction

u_{k-1} Process inputs from t_{k-1} to t_k

V Covariance matrix for process noise

v_k Process noise

W Covariance matrix for measurement noise

w_k Measurement noise

x_k Model state vector at time t_k

y_k Measurement vector at time t_k

z_k Output vector at time t_k (CV)

Reaction Symbols

(i) Slag component i

$[i]$ Metal component i

$\%wt_i$ Mass percent of species i

ϵ Dilution factor

γ Raoultian activity coefficient

a_i Activity

f_i Henry's activity coefficient

K Equilibrium constant

k Rate constant [-]

L_i Partition ratio of species i

$p_{CO,0}$ Reference pressure of CO

p_{CO} Partial pressure of CO

r_i Reaction rate [mol/s]

x_i Molar fraction of species i

B Ratio of basic- and acidic oxides

Thermodynaic Symbols

A Area [m^2]

C_p Heat capacity J/K

F_i Molecular flow [mol/s]

G Gibbs free energy [J]

H Enthalpy [J]

h_c Heat transfer coefficient $[W/m^2K]$

k Thermal conductivity $[W/mK]$

m Mass [kg]

M_i Molecular weight [kg/mol]

Q Volume flow $[m^3/s]$

q Heat transfer [J/s]

R Gas constant [J/molK]

S Entropy [J]

T Temperature [K]

V Volume [m^3]

w Mass flow rate [kg/s]

x Distance

Chapter 1

Introduction

This thesis presents a full model of a Basic Oxygen Furnace (BOF). The results are validated against data from a plant at SSAB, Raahe. The model includes off-gas modelling and continuous lining temperature, in addition to reaction rates and heat and mass transfer between the different control volumes. Furthermore, a Moving Horizon Estimator (MHE) together with a Nonlinear Model Predictive Control (NMPC) has been implemented. The results from the estimator and NMPC are presented and discussed. As the model used in this thesis was first developed in the preliminary project thesis, some parts are included such that the thesis contains a more complete description. These include, Process Modelling Theory, section 2, and parts of Modelling, section 4.

1.1 Steelmaking

Steel is and has been for the last two centuries the most important material in construction and engineering (World Steel Organisation, n.d.). In 2016 a total of 1.6 billion tons of crude steel were produced in the world, and the production is rising. Steel is composed of many different species but mainly consists of iron. Adjusting the amounts of various alloys one can achieve different steel grades and properties. Carefully adjusting the components in the steel the producer can tailor the product properties such as strength, ductility and durability. The steelmaking process occurs after the production of pig iron and is categorised into three different stages, primary steelmaking, secondary steelmaking and casting. Primary steelmaking produces the crude steel, where its composition and purity is refined. This thesis focuses on the primary steelmaking stage.

The production of steel has evolved greatly from the industrial production in the late 19th century. Initially, steel was made either through the open hearth, or the Bessemer steelmaking process. These were the two methods of production until the discovery of basic oxygen steelmaking was introduced in the 1960's. Today, there are mainly two ways of producing steel, by Electric Arc Furnace (EAF) or BOF as

presented in Figure 1.1. The EAF is charged with recycled scrap metal and other raw materials, and uses electric power to melt the scrap. During melting other metals can be added, and as with the basic oxygen process, oxygen is blown into the furnace to purify the steel. BOF is charged with molten metal and recycled scrap metal, and exploits the heat from the exothermic oxidising reactions in the converter. In a Linz-Donawitz process, an oxygen lance is used to blow oxygen into the carbon-rich hot metal. The hot metal bath is often a mixture of molten metal and recycled scrap. The oxygen reacts with carbon creating CO and CO_2 gas, and other impurities creating the slag phase on top of the bath. This, together with the slag reactions, reduces the carbon content in the hot metal down below 1%, turning it into molten steel.

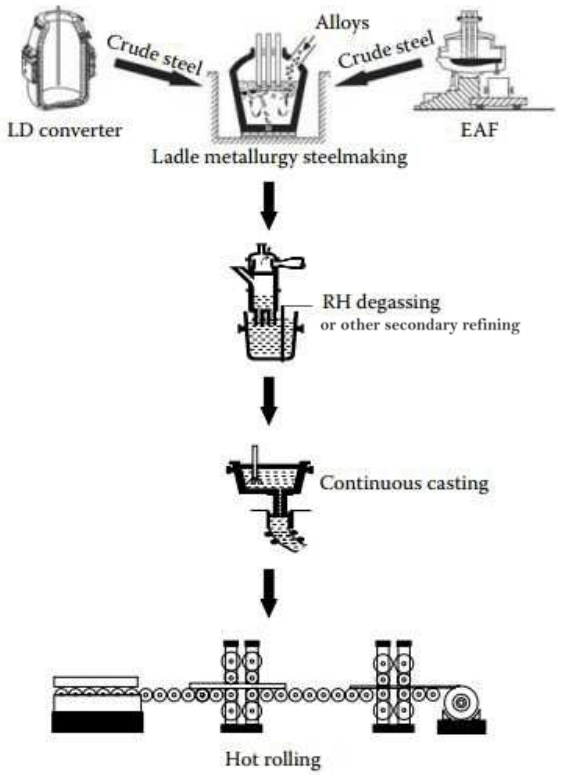

Figure 1.1: Two main steelmaking routes (Mazumdar and Evans, 2010)

1.2 Basic Oxygen Steelmaking

Molten iron is charged into the converter from a blast furnace, where the metal is refined under an oxidising and basic environment (Mazumdar and Evans, 2010). The oxidising of molten iron is ensured by blowing pure oxygen, $\approx 99\%$, into the

molten iron by using lance which injects the oxygen with a sonic velocity. The sonic velocity allows the oxygen to enter the bath, ensuring bath agitation and enables the oxidising reactions. The height of the lance and velocity of the oxygen jet are important factors in the steelmaking process. The jet penetration is crucial in ensuring agitation and for the efficiency of the oxidising reactions. Insufficient jet penetration causes large amounts of oxygen to escape from the bath. The penetration impacts the stirring, ensuring that the impurities are transferred to the jet impact area of the bath. Lack of stirring forces will lead to heterogeneity between the impact area and the bath. Stirring forces also impacts the reaction between the slag phase and metal phase as these are dependent on the arrival of reactants to the slag-metal interface. Typical design of a BOF converter is presented in Figure 1.2.

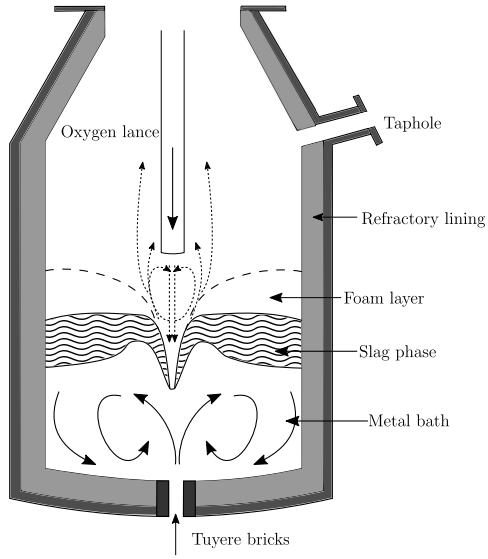

Figure 1.2: Typical design of an BOF converter

The procedure of producing steel via basic oxygen furnace starts by charging scrap into the converter followed by hot metal from the blast furnace. The amount of scrap relative to the amount of hot metal varies with each producer but is often in the range 10-30%. In addition to scrap, fluxes (chemical purifying agents) such as iron ore (pellets), lime and other additions can be included from the start. These are often added during blowing to improve the slags basicity or the slag and metal's composition. The basicity of the slag, the ratio between basic oxides and acidic oxides (i.e. CaO and SiO_2), is an essential factor in basic oxygen steelmaking. The basicity of the slag influences slag reactions and high basicity prevents the slag from being corrosive against the lining. After adding scrap, additives and hot metal, the lance is lowered and injects oxygen into the bath. The reactions between oxygen and metal, the formation of slag and dissolution of additions start

immediately. The temperature of the impact area and slag increases rapidly by the released heat from the oxidising reactions. During the blowing period, the lance height and oxygen flow are adjusted to control the oxidation rates to achieve the desired characteristics. In order to improve the homogeneity of the bath and improve the oxygen utilisation, the converter is injected with inert gases in the bottom. These inert gases are typically N_2 and Ar. After the blow, if the steel grade is not accepted, the operator can start blowing again. Otherwise, the steel is tapped to a steel ladle for the secondary steelmaking stage. Slag is emptied, and the lining is inspected before the next heat. A typical batch is presented in Figure 1.3.

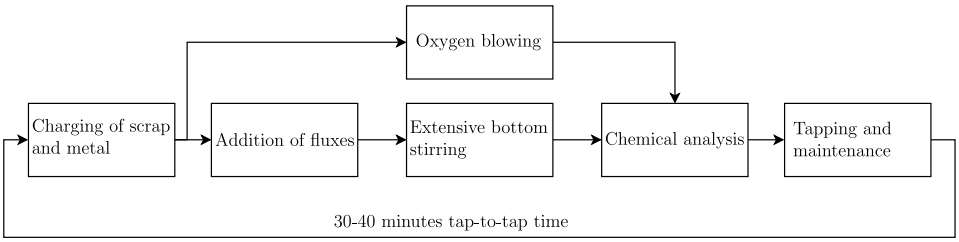

Figure 1.3: Operation sequence in basic oxygen steelmaking

Due to the hostile environment in a steelmaking process, there are few measurements available. At some plants, a sub-lance can be lowered towards the end of the main blow to measure exact composition and temperature, but this varies from plant to plant. There have been several studies on implementing new measurement technologies to get time series data on the bath, but this is yet to be implemented. The most common method of measuring time series data is using the waste gas. Using waste gas measurements, the operator can extract information about the bath by using chemical analysis of the gas as well as the temperature.

Although inaccuracies in the model can be compensated for in certain control methods, an accurate model is preferred for better result and with the lack of online measurements. The goal of an accurate modelling is to implement a control strategy that can lead to more precise and cost-effective production of steel. In addition to the quality and cost of steelmaking, more strict environmental constraints, force the companies to produce better steel at less cost with less emissions.

1.3 Process Control and Estimation

Advanced process control and estimation have excelled the last couple of decades. In many processing industries model predictive control has become the most popular advance control method. The recent advances in computational power have made it possible to do online optimisation, instead of doing an offline optimisation prior to the process. With the steel industry's hostile environment, and in particular the BOF process, there are few and infrequent measurements available. This

has led to that the process has been operated based on experience and the accuracy of the previous batches. With model predictive control and a moving horizon estimator it may be possible to increase the efficiency and reduce both costs and emissions.

Model Predictive Control (MPC) is a form of control where the optimal control action is calculated online. For each sample, the MPC solves a finite horizon optimal control problem where the initial state is the current state of the system. The first input in the sequence is applied to the system. MPC was initially developed to meet the specific control needs of power plants and refineries, but can now be found in many areas such as chemical, automotive and aerospace (Qin and Badgwell, 2003). The development of MPC began in the 1960's with Rudolph Kalman's development of the linear quadratic regulator, designed to minimise a quadratic objective function. The Linear Quadratic Gaussian controller was a powerful tool in process control with its ability to estimate the plant's state from noisy measurements. Although the LQG was a powerful and robust controller, it lacked the ability to handle constraints and process non-linearities. The LQG and the development of the maximum principle, dynamic programming and numerical optimisation methods paved the way for the MPC and its non-linear version. The non-linear MPC handles these strong non-linearities. However, the non-linear optimisation problems are often non-convex, and the convergence and success of the optimisation are highly dependent on the initial guess (Johansen, 2011).

An MPC controller needs a reasonably accurate estimate of the process' state. Due to model errors and disturbances, it is necessary to update the model. There are many different kinds of state estimators, the most common and widespread is the Kalman filter, with the unscented and extended version. This has gained its popularity due to its simplicity and efficiency. However, with the BOF process non-linearity, constraints and few measurements, a moving horizon estimator (also known as receding horizon estimator), is preferable. The basic strategy of MHE is to estimate the state using a moving, fixed-size window of data. When a new measurement is available, the oldest measurement is removed from the window, and the new measurement is added.

With the few and infrequent measurements for the BOF process and the highly nonlinear model, a moving horizon estimator is more suitable. In addition, the MHE supports delayed measurements, which is beneficial with the measurements from chemical analysis of the metal. The principle behind MHE is presented in Figure 1.4. At time T, the estimator only considers the previous N samples in the horizon, while summarising the prior data in the objective function.

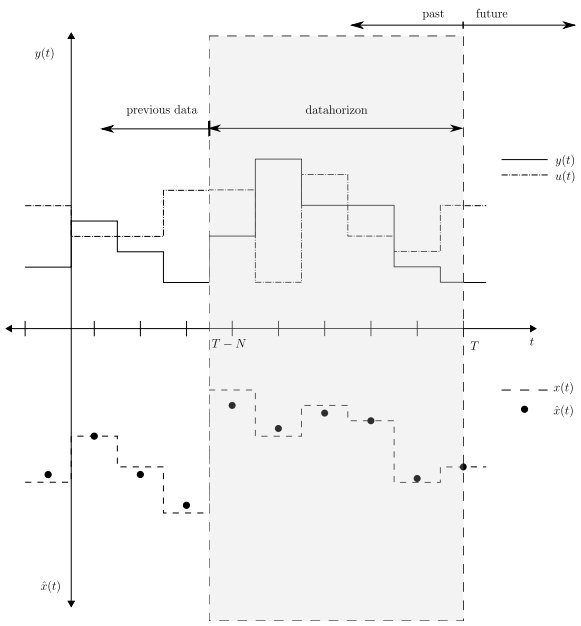

Figure 1.4: Princple of MHE

1.4 Previous Work

Much work has been done regarding modelling different aspects of the BOF process, though there has not been done much work in creating a complete model of the process. Hammervold made a model of the Linz-Donawitz converter and further developed this while creating an NMPC for the converter (Hammervold, 2010). During this modelling, he created a comprehensive model describing a Linz-Donawitz converter. Kruskopf and Visuri (2017) created a BOF model based on Gibbs' energy minimisation. Sarkar et al. (2015*a*) made a model of an LD converter, also by using Gibbs' energy minimisation. The result from Hammervold's model showed a good validity compared to the simulation tool at SteelUniversity.org and the proposed process characteristic in literature such as in Turkdogan (2010). Kruskopf and Visuri validated their results against measurements from an industrial-scale converter. Their results showed to be well correlated with the measured values and against the models proposed in literature. Comparing Kruskopf and Visuri (2017) with Sarkar et al. (2015*a*), their slag composition during the heat is quite different, Kruskopf and Visuri (2017) slag composition fits the measurements better than the model presented in Sarkar et al. (2015*a*). Dogan et al. (2011*a*) (Dogan et al. (2011*b*), Dogan et al. (2011*c*)) made a comprehensive model including scrap melting, dissolution of fluxes and slag chemistry. Their final results showed a good approximation compared to process data.

Concerning control and estimation, there have not been many studies on BOF. Hammervold (2011) further developed his model from (Hammervold, 2010) and

investigated the control performance using a Kalman filter and an MPC. With the late development of better artificial intelligence and more specific machine learning algorithms, there have been some studies on implementing this on a BOF process. Han and Liu (2014) used machine learning techniques to predict the endpoint measurements in the molten steel such as temperature and carbon content. The results indicated good prediction accuracy and had good application prospects. Han et al. (2014) presented a model for the control of BOF oxygen volume and additives based on information theory and AI technology. Again, the model showed good results. This is outside the scope of this thesis but is mentioned to identify the potential future options.

1.4.1 Previous Related Work by the Author

The work on this project started as an internship position at Cybernetica AS during the summer of 2017. The work was continued throughout the fall as a project assignment at NTNU. During this work, a first principle model and a thermodynamic library were developed. The model included an initial design of the control volumes in the bath, reaction kinetics between oxygen and metal, and between slag and metal. In addition, bottom stirring and cooling of the off-gas was implemented. The model in this work has been further developed in terms of more accurate modelling of the off-gas system, improved reaction kinetics between slag and metal and the implementation of bottom stirring efficiency, emulsion height and continuous monitoring of converter lining temperature. In addition, the implementation of MHE and NMPC has been studied. The previous work is presented in Dyrdal (2017).

1.5 Outline of Thesis

The work in this thesis is related to a larger project where Cybernetica AS is the supplier of the control system. The goal of this study is to create a comprehensive model that reproduce the process behaviour and check the improvements by configuring Cybernetica's interfaces for model predictive control and moving horizon estimator. By using process data from SSAB Raahe, the results are controlled and validated. This data is also essential in adjusting the parameters used in the model. The estimation and control of the process are demonstrated by using simulated data.

The thesis is divided into Process Modelling Theory, Control Theory, Modelling, Predictive Monitoring and at the end Overall Conclusions and Further Work. The process modelling theory section contains the underlying theory that is needed to understand the physics and chemistry behind the modelling and the results. Control theory presents the theory behind the implementation of the controller and estimator. Modelling includes the calculations in the model as well as the design. Predictive monitoring presents how the controller and estimator are configured for this model. Results, discussion and conclusions for modelling and predictive monitoring is added at the end of its respective chapter. Finally, the overall con-

clusions and further work contains a summary of the conclusions and suggested improvements for the model, estimation and control.

Chapter 2

Process Modelling Theory

During steelmaking there are numerous different physical and chemical processes. The processes such as melting, chemical reaction and separation involves multi phase flow, chemical kinetics, rate phenomena etc. In order to create a valid and accurate model, one needs sound knowledge in these fields. In this chapter the theory behind the modelling of the process is presented, and the theory needed to understand the process chemistry and reaction rates. The following section is from the preliminary project thesis and is included to create a more complete report.

2.1 Thermodynamics

2.1.1 First Law of Thermodynamics

The first law of thermodynamics is based on the concept of conservation of energy, when one system interacts with another system, the gain of energy in one system is the loss of the other.

Enthalpy of Reaction The enthalpy change due to a reaction is given by the difference in enthalpies of the products and reactants. For an isobaric and isothermal reaction,

$$A + B \rightarrow C + D$$

the enthalpy change is given by:

$$\Delta H = (\Delta H_C^\circ + \Delta H_D^\circ) - (\Delta H_A^\circ + \Delta H_B^\circ) \tag{2.1.1}$$

2.1.2 Second Law of Thermodynamics

The law of dissipation of energy states that all natural processes occurring without external interference are irreversible (Turkdogan, 2010). A spontaneous process cannot be reversed without any change in the system brought about by external interference. In ideal cases where the system is at equilibrium or undergoing a reversible process, the total entropy can remain constant, an increase in total entropy accounts for the irreversibility of natural processes. The change in entropy, ΔS, is defined such that for any isobaric and isothermal reversible process,

$$\Delta S = \frac{dH}{T} = \frac{C_p}{T} dT = C_p d(\ln T) \tag{2.1.2}$$

2.1.3 Third Law of Thermodynamics

The third law of thermodynamics state that the entropy of any homogeneous or ordered crystalline substance, which is in internal equilibrium, is zero at absolute zero temperature. Hence, the equation 2.1.2 has a finite value at a temperature T

$$S_T = \int_0^T C_p d(\ln T) \tag{2.1.3}$$

The entropy of reaction is

$$\Delta S = \sum S(products) - \sum S(reactants) \tag{2.1.4}$$

2.1.4 Gibbs Free Energy

Combining the first and second law, Gibbs derived the free energy equation for a reversible process at constant pressure and temperature

$$G = H - TS \tag{2.1.5}$$

The variation of the standard free energy change with temperature is given by:

$$\Delta G_T^\circ = \Delta H_{298}^\circ + \int_{298}^T \Delta C_P dT - T\Delta S_{298}^\circ - T\int_{298}^T \frac{\Delta C_P}{T} dT \tag{2.1.6}$$

For many reactions the temperature dependence of ΔH° and $\Delta\ S^\circ$ are similar and tend to cancel each other, hence the nonlinearity of ΔG° with temperature is minimized. Using average values for enthalpy and entropy, the free energy simplifies to:

$$\Delta G^\circ = \Delta H^\circ - \Delta S^\circ T \tag{2.1.7}$$

2.2 Reaction Rates

2.2.1 Chemical Kinetics

The reaction between adsorbed species L and M on the surface, i.e. interface between slag and metal, producing product Q occurs via the formation of an activated complex $(LM)^*$.

$$L + M = (LM)^* \rightarrow Q \tag{2.2.1}$$

In terms of a single rate constant, the net reaction rate is formulated as

$$\frac{dn}{dt} = \hat{k}(a_L a_M - (a_L a_M)_{eq}) \tag{2.2.2}$$

where $\hat{k}$ is the isothermal rate constant of the forward reaction and a_i is the activity of species i. By using Arrhenius' equation, the reaction rate becomes

$$\frac{dn}{dt} = ke^{\frac{-E_0}{RT}}(a_L a_M - (a_L a_M)_{eq}) \tag{2.2.3}$$

where E_0 is the activation energy, R is the universal gas constant.

2.2.2 Reaction Equilibrium Constant

Considering the following isobaric and isothermal reaction

$$mM + nN = uU + vV \tag{2.2.4}$$

The equilibrium constant is defined by the following relation:

$$K = \frac{(a_U)^u (a_V)^v}{(a_M)^m (a_N)^n} \tag{2.2.5}$$

where a_i^k is the corresponding activity coefficient for the species, i, and k is the stoichiometry of reaction. By using the free energy change, the equilibrium constant can be derived:

$$\Delta G^\circ = -RT \ln K \tag{2.2.6}$$

2.2.3 Activity of Solutes

Using equation 2.1.5 together with the definition of enthalpy and entropy for a system doing work only against pressure, the change in Gibbs free energy can be expressed as (Turkdogan, 2010),

$$dG = VdP - SdT \tag{2.2.7}$$

At constant temperature and for an ideal gas mixture,

$$dG_i = RTd(lnp_i) \tag{2.2.8}$$

where p_i is the partial pressure of vapor i. For nonideal solutions we can define the activity of species, i, as

$$a_i = \frac{p_i}{p_i^\circ} \tag{2.2.9}$$

where p_i° is the partial pressure of pure component i

Raoult's Law
Raoult's law explains the relationship between vapour pressure of a solution and the partial pressure of solutes in that solution. The law states that for an ideal solution, $a_i = x_i$, where x_i is the mole fraction. In order to account for deviations from the ideal solution, we introduce the Raoultian activity coefficient

$$\gamma_i = \frac{a_i}{x_i} \tag{2.2.10}$$

The variations of activity with respect to mole fraction in an ideal or nonideal solution are shown in Figure 2.1.

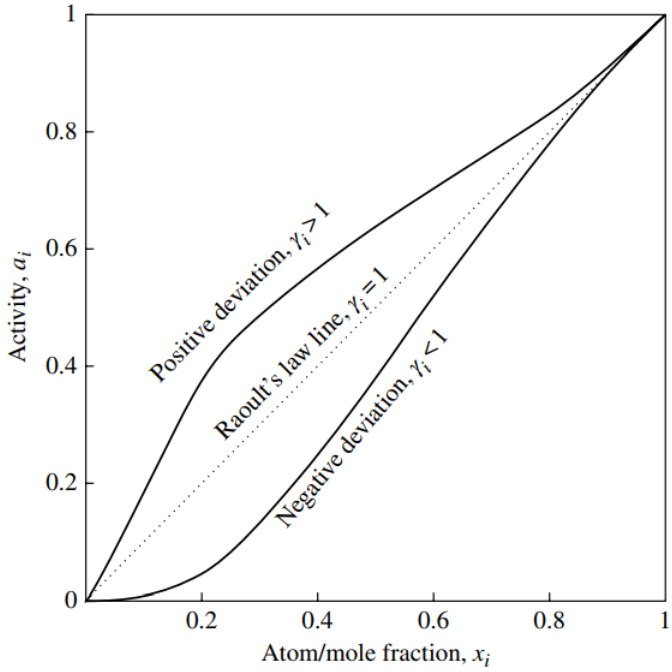

Figure 2.1: Deviations from Raoult's ideal behaviour (Shamsuddin, 2016).

Henry's Law
Raoult's law tends to approximate the real behaviour of the solvent in a dilute solution, while Henry's law approximates the real behaviour at very low concentration.

Henry's law states that for infinitely dilute solutions, the activity is proportional to the concentration,

$$a_i = \gamma_i^\circ x_i \tag{2.2.11}$$

Since Henry's law is only valid for infinitely dilute solutions, the Henry's activity coefficient is used to measure the deviation from Henry's law.

$$f_i = \frac{\gamma_i}{\gamma_i^\circ} \tag{2.2.12}$$

Partition Ratio
In some solutions, it may be beneficial to describe the equilibrium of the species by using the partition ratio. The partition ratio between slag and metal is an index of species holding capacity in the slag, which determines the content of species achievable in the steel. The partition ratio is defined as,

$$L_i = \frac{(\%wt_i)}{[\%wt_i]} \tag{2.2.13}$$

where $\%wt_i$ is the mass percent of species i, parenthesis and brackets denote slag- and metal phase, respectively.

2.3 Slag chemistry

Slag is a mixture of various oxides and is produced during blowing of oxygen. Additions as lime, dolomite and iron ore are used to increase the concentration of oxides such as calcium oxide, iron oxide or magnesium oxide. This phase plays an important role in steelmaking, as slag helps remove impurities from the steel and protect the lining of the converter. Since the slag phase is composed of several oxides, their states are expressed using ternary or pseudoternary diagram. Information from these diagrams is essential when designing and optimising a process. The liquidus temperature is an important factor for the engineer, as it is essential to maintain a liquid slag (Seetharaman et al., 2014). Most common oxides in slags are FeO, CaO, SiO_2 and MgO. These are for low-phosphorous processes 88% to 92% of the total concentration. Hence, the simplest type of steelmaking slag to be considered is the CaO-MgO-FeO-SiO_2 quaternary system (Turkdogan, 2010). A ternary diagram of a CaO-SiO_2-FeO system is presented in Figure 2.2.

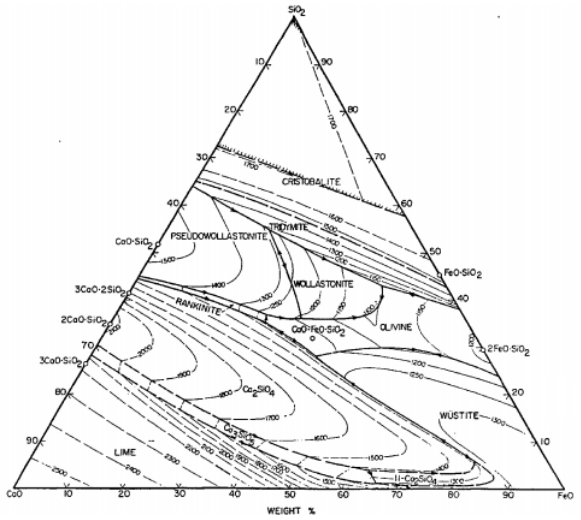

Figure 2.2: Liquidus isotherms of CaO-SiO_2-FeO system (Turkdogan, 2010).

In Figure 2.3 the system CaO-SiO_2-FeO has four two-phase regions, dotted lines, two three-phase regions and one liquid region.

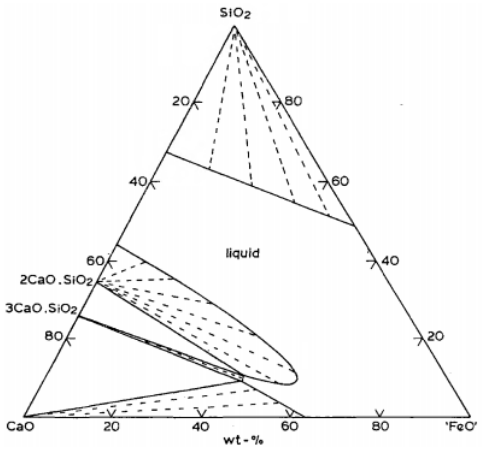

Figure 2.3: Phase equilibria with liquid iron at 1600℃(Turkdogan, 2010).

The activities in the slag are influenced by the composition in the slag, as well as the temperature. The oxide activities in a CaO-FeO-SiO_2 system is presented in Figure 2.4.

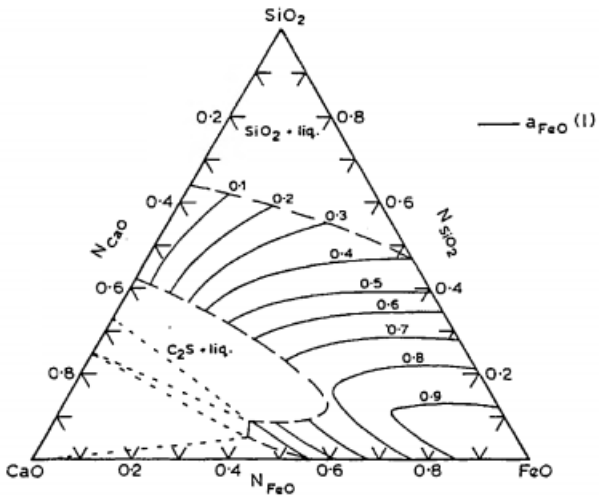

Figure 2.4: Activities of iron and calcium oxide and silicon dioxide at 1550°C(Turkdogan, 2010).

The basicity, the ratio of basic and acidic oxides in the slag, used in this model is the lime basicity, given by

$$B = \frac{\%CaO}{\%SiO_2} \tag{2.3.1}$$

As presented in Figure 2.5, the activity of iron oxide is highly influenced by the basicity of the slag.

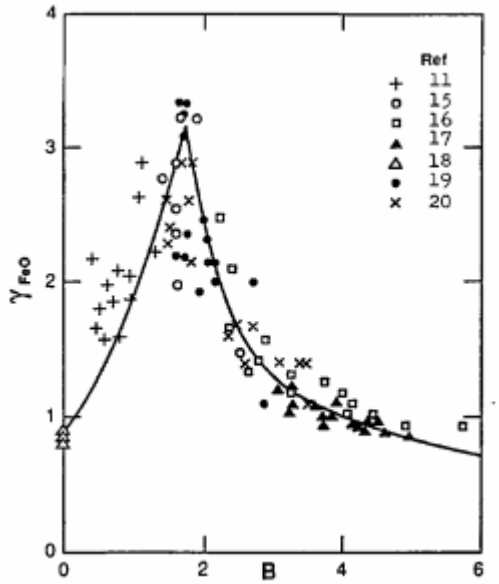

Figure 2.5: Activities of iron oxide with regards to slag basicity at 1600℃(Turkdogan, 2010).

2.4 Mass Balance

The mass of a material volume is

$$m = \iiint_{V_m(t)} \rho \, dV \tag{2.4.1}$$

Hence the principle of mass conservation can be expressed as

$$\frac{D}{Dt} \iiint_{V} \rho \, dV = 0 \tag{2.4.2}$$

For a fixed volume the mass balance then becomes

$$\frac{d}{dt} \iiint_{V_f} \rho \, dV = - \iiint_{\partial V_c} \rho v^\top n \, dA \tag{2.4.3}$$

where v is the flow velocity and n is the unit normal vector pointing out.

2.5 Energy Balance

The law of conservation of energy states that for an isolated system within a frame of reference, the total energy of the system is conserved.

For a fixed volume the energy balance can be written on integral form as

$$\frac{D}{Dt}\iiint_V \rho e \, dV = \frac{d}{dt}\iiint_V \rho e \, dV + \iint_{\partial V} \rho e v^\top n \, dA \tag{2.5.1}$$

This equation can be expressed in words as,

$$\left\{\begin{array}{c}\text{Rate of change}\\ \text{of total}\\ \text{energy inside V}\end{array}\right\} = \left\{\begin{array}{c}\text{Rate of change}\\ \text{due to changes}\\ \text{within V}\end{array}\right\} + \left\{\begin{array}{c}\text{Rate of change due to movement}\\ \text{on the surface A of the}\\ \text{body or through heat transfer}\end{array}\right\} \tag{2.5.2}$$

The total energy, e, is defined as

$$e = u + \frac{1}{2}v^2 + \phi \tag{2.5.3}$$

where u is the specific internal energy

$$u = h + \frac{p}{\rho} \tag{2.5.4}$$

$\frac{1}{2}v^2$ is the specific kinetic energy and ϕ is the specific potential energy (Egeland and Gravdahl, 2002). Assuming that the kinetic and potential energy for the system is negligible, then $e = u$ energy balance can be written as

$$\Delta E = E_{in} - E_{out} \tag{2.5.5}$$

For this kind of converters it is a fair assumption as the total energy is dominated by the enthalpy. A 100 ton converter has a specific potential energy of $13.73\frac{J}{kg}$ compared to the specific enthalpy of iron which is $1023.15\frac{kJ}{kg}$ at 1500°C.

2.6 Heat Transfer

There are three elementary modes of heat transfer, conduction, radiation and convection. By using these forms of heat transfer, the amount of heat transferred to the surrounds as well as the heat transferred to the solid scrap can be calculated.

Radiation Radiative heat transfer is electromagnetic waves generated by the thermal motion of the material. The propagation of the electromagnetic waves is a result of the difference in temperature between the body and surroundings. The amount of heat lost due to radiation can easily be calculated using Stefan-Boltzmann's law of thermal radiation (Mazumdar and Evans, 2010).

$$q_{rad} = \sigma_R A \theta^4 \tag{2.6.1}$$

Where σ_R is the Stefan-Boltzmann constant, A is the area and θ the temperature of the body. This equation is with the assumption that the surface is completely black. To take this into account, the emissivity is introduced. By also introducing

the surrounding temperature, the radiation absorbed by the environment is also taken into account. Then the radiative heat transfer can be expressed as,

$$q_{rad} = \sigma_R \epsilon_S A(\theta_S^4 - \theta_{\text{inf}}^4) \tag{2.6.2}$$

Where ϵ_S is the emissivity of the surface, for non-black surfaces less than zero and θ_S and θ_{inf} is the surface- and surrounding temperature, i.e. room temperature.

Conduction Heat transfer by conduction is simply the transfer of energy by molecules movement from a part with higher temperature to a part with lower temperature. Conduction plays a crucial role in the melting of additions and scrap, where the heat is continuously transferred to the "colder" parts of the body. By using Fourier's law, the rate of heat transfer by conduction can be calculated for the x-direction (normal to the surface A), by (Mazumdar and Evans, 2010):

$$q_{c,x} = -kA\frac{\partial T}{\partial x} \tag{2.6.3}$$

Where k is the thermal conductivity, A area, T temperature and x is the length variable.

Convection Convective heat transfer is the heat transfer from the movement of a fluid. The governing equation of calculating convection is based on a rigorous way of calculating the heat transfer coefficient, and this is more complex than what is needed for this model. Therefore a simpler equation with a constant coefficient is implemented for the heat transfer calculation.

$$q_{conv} = h_c A(T_{\text{inf}} - T_S) \tag{2.6.4}$$

In which h_c is heat transfer coefficient, A surface area, and $T_{\text{inf}} - T_S$ is the temperature difference in the flow.

Chapter 3

Control Theory

This chapter presents the underlying control theory for understanding the configuration of the moving horizon estimator and the model predictive control.

3.1 Moving Horizon Estimator

In most processes, the measurements are only a small subset of all the states necessary to model the system. In addition, the measurements and the state evolution is affected by measurement noise and process noise. The challenge for the state estimator is to determine a good state estimate to be used in the regulator, in the presence of noise and incomplete information. The most well known and established estimator is the Kalman filter (KF) and its non-linear version, extended Kalman filter (EKF). The Kalman filter is the optimal estimator when the white noise has a Gaussian probability distribution. The extended Kalman filter has received much attention, mainly due to its simplicity and its effectiveness in handling non-linear systems. However, there are some drawbacks with the EKF, the full knowledge about the process noise is rarely met in practice, and large initial state errors lead to inaccurate estimation and potential estimator divergence (Rawlings and Mayne, 2009). With the few and infrequent measurements for the BOF process, a moving horizon estimator is more suitable. In addition, the MHE supports delayed measurements, which is beneficial with the measurements from chemical analysis of the metal.

The moving horizon estimator (MHE) has become popular in recent years due to its ability to handle explicitly non-linear systems and constraints. The basic idea of MHE is to reformulate the estimation problem as a quadratic programming problem using a fixed size, moving estimation window (Rao et al., 2001).

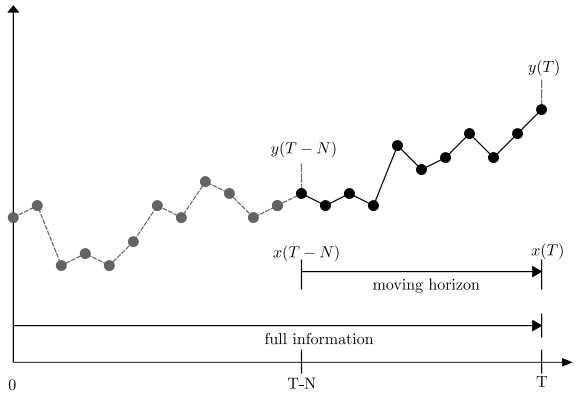

Figure 3.1: The moving horizon estimation problem

MHE only considers the N most recent measurements and find the most recent N values of the state trajectory, as presented in Figure 3.1.

For a linear time-invariant discrete and unconstrained system, the state estimation problem is defined as,

$$\begin{aligned} &\Phi_T^* = \min_{x_0,\ldots,x_T} \Gamma(x(0)) + \sum_{k=0}^{T-1} l_k \\ &\text{subject to} \\ &x_{k+1} = f(x_k, u_k, v_k) \\ &y_k = g(x_k) + w_k \\ &x_k \in \mathbb{X}_k, v_k \in \mathbb{V}_k, w_k \in \mathbb{W}_k \end{aligned} \tag{3.1.1}$$

where Φ_T is the arrival cost. We define the stage cost, l_k, as,

$$l_k(w_k, v_k) = w_k^\top W_k^{-1} w_k + v_k^\top V_k^{-1} v_k \tag{3.1.2}$$

W_k and V_k is the covariance matrix for the measurement and process noise, respectively. Both matrices are symmetric positive definite.

If the system is linear, $f(x_k, u_k, w_k) = A_k x_k$ and $g(x_k) = C_k x_k$, the prior weighting on state at time $T = 0$, $\Gamma(x(0))$ is defined as,

$$\Gamma(x(0)) = (x_0 - \hat{x}_0)^\top \Pi_0^{-1} (x_0 - \hat{x}_0) \tag{3.1.3}$$

The pair (x_0, Π_0) summarizes the prior information at time $T = 0$ and is part of the data of the state estimation problem (Rao et al., 2001). If the system in addition is unconstrained and the cost function is quadratic the solution is found recursively using the matrix Riccati equation 3.1.4,

$$\Pi_{k+1} = G_k V_k G_k^\top + A_k \Pi_k A_k^\top - A_k \Pi_k C_k^\top (W_k + C_k \Pi_k C_k^\top)^{-1} C_k \Pi_k A_k^\top \tag{3.1.4}$$

with the initial condition Π_0.

Consider the full information problem in Equation 3.1.1, the problem can be rearranged into two pieces,

$$\Phi_T^*(x_0, \{v_k\}_{k=0}^{T-1}) = \min \Phi_T(x_0, \{v_k\}_{k=0}^{T-1}) = \min \Phi_{T-N}(x_0, \{v_k\}) + \sum_{k=T-N}^{T-1} w_k^\top W_k^{-1} w_k + v_k^\top V_k^{-1} v_k \tag{3.1.5}$$

using forward dynamic programming, the following equivalence can be established (Rao et al., 2001),

$$\min_{x_0, \{v_k\}_{k=0}^{T-1}} \Phi_T(x_0, \{v_k\}) = \min_{z, \{v_k\}_{k=T-N}^{T-1}} \sum_{k=T-N}^{T-1} w_k^\top W_k^{-1} w_k + v_k^\top V_k^{-1} v_k + (x_{T-N} - \hat{x}_{T-N})^\top \Pi_{T-N}^{-1} (x_{T-N} - \hat{x}_{T-N}) + \Phi_{T-N}^* \tag{3.1.6}$$

For a non-linear and constrained system, an algebraic expression for the arrival cost rarely exists. One reasonable solution is to approximate the arrival cost for the constrained problem with the arrival cost for the unconstrained problem. However, if the arrival cost is poorly approximated, instability may arise. For a constrained non-linear system the MHE problem from $T - N$ to T is defined as,

$$\hat{\Phi}_T^* = \min_{x_{T-N}, \ldots, x_T} \Gamma(x(T-N)) + \sum_{k=T-N}^{T-1} l_k \tag{3.1.7}$$

with prior weighting on state at time $T = T - N$ being,

$$\Gamma(x(T-N)) = (x_{T-N} - \hat{x}_{T-N})^\top \Pi_{T-N}^{-1} (x_{T-N} - \hat{x}_{T-N}) + \hat{\Phi}_{T-N}^* \tag{3.1.8}$$

The MHE cost $\hat{\Phi}_T^*$ approximates the full information cost Φ_T^* by replacing Φ_{T-N}^* with the approximation $(x_{T-N} - \hat{x}_{T-N})^\top \Pi_{T-N}^{-1} (x_{T-N} - \hat{x}_{T-N}) + \hat{\Phi}_{T-N}^*$. The pair (x_{T-N}, Π_{T-N}) summarizes the prior information at time $T = T - N$ and the state vector $\hat{x}_{T-N}$ is the moving horizon estimate at time $T - N$, while Π_{T-N} is the solution to the matrix Ricatti equation 3.1.4 subject to the initial condition. For $T \leq N$ the MHE estimate is equal to the full information estimate, $\hat{\Phi}_T = \Phi_T$ (Rao et al., 2001). For details regarding the stability of the estimator the reader is referred to Rao et al. (2003).

3.2 Model Predictive Control

Model predictive control has become a common regulator in many industries such as refineries, chemicals, food processing and metallurgy. Model predictive control builds on the concepts from optimal controller design. The combined LQR and Kalman filter, LQG, was a powerful solution to control a process but lacked the support of non-linear models with uncertainties and constraints. Model predictive control handles these systems and dynamically optimises the input over a prediction horizon. A system with an MPC controller and estimator is presented in Figure 3.2.

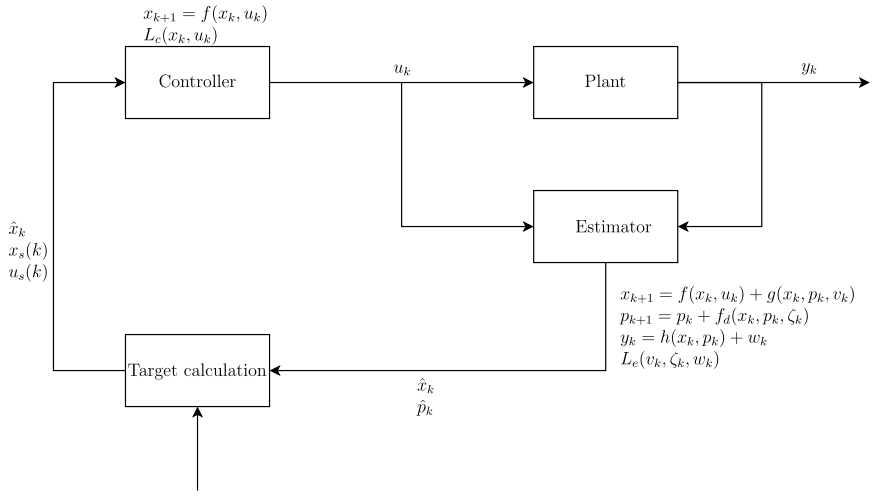

Figure 3.2: System with estimator and controller

A standard MPC optimisation problem takes the form,

$$\min_u J(x,u) = \sum_{k=0}^{N-1} \frac{1}{2}\{(x_k - x_{ref,k})^\top Q(x_k - x_{ref,k}) + (u_k - u_{ref,k})^\top P(u_k - u_{ref,k})\} + (x_N - x_{ref,N})^\top S(x_N - x_{ref,N}) \tag{3.2.1}$$

subject to

$$\begin{aligned} &x_{k+1} = A_k x_k + B_k u_k + G v_k \\ &X_L \leq x_i \leq X_U, \text{ for } 0 \leq i \leq n+j \\ &U_L \leq u_i \leq U_U, \text{ for } 0 \leq i \leq n+j \\ &Y_{L,i} \leq y_i \leq Y_{U,i}, \text{ for } 1 \leq i \leq n+j \end{aligned} \tag{3.2.2}$$

The matrices Q and P contain the weights that penalize deviations from the reference trajectory of states and inputs. The matrices P and S are assumed to be symmetric positive definite, whereas Q is assumed to be symmetric semi-positive definite. It may also be preferable to add constraint on the rate of change of the inputs, $\Delta U_L \leq u_k - u_{k-1} \leq \Delta U_U$. The principle of MPC is illustrated in Figure 3.3.

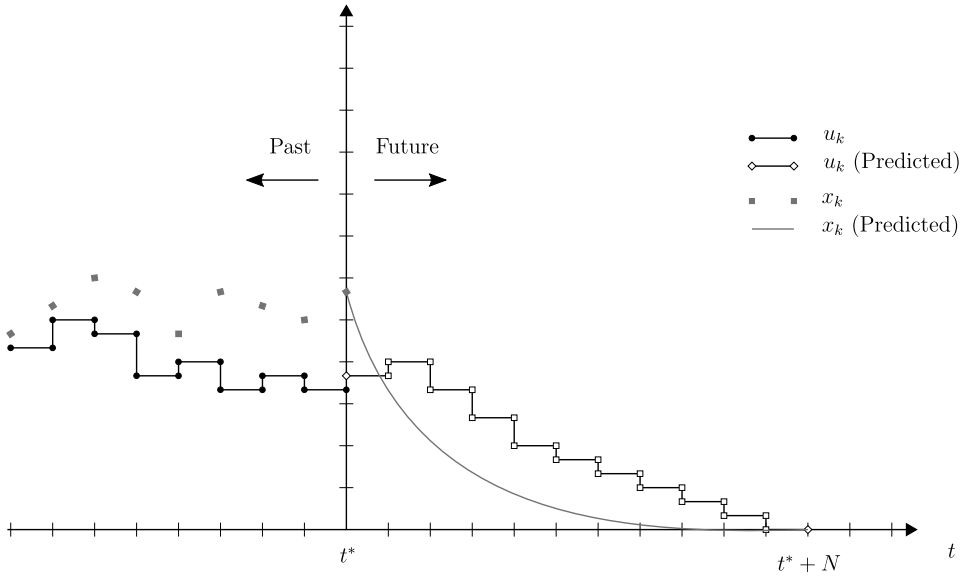

Figure 3.3: The MPC principle

The MPC algorithm gets the state estimate at time t^* and solves the open loop problem. The future control inputs are the solution to the open loop optimisation problem at time t^*. The MPC algorithm can be summarized as (Foss and Heirung, 2016),

for $k = 0, 1, 2...$ **do**
Compute an estimate of the current state $\hat{x}_k$ based on the measured data up until time t^*.
Solve a dynamic optimization problem on the prediction horizon from t^* to t^*+N with $\hat{x}_k$ as the initial condition.
Apply the first control move u_k from the solution above.
end for

3.2.1 Non-linear MPC

Given a system $x_{k+1} = f(x_k, u_k)$ and $y_k = g(x_k)$, in which f is twice continuously differentiable. System is subject to constraints on both states and control. The optimal control problem defined in equation 3.2.1 can be rewritten as,

$$\min_u J(x,u) = \sum_{k=0}^{N-1} \frac{1}{2}\{(x_k - x_{ref,k})^\top Q(x_k - x_{ref,k}) + (u_k - u_{ref,k})^\top P(u_k - u_{ref,k})\} + (x_N - x_{ref,N})^\top S(x_N - x_{ref,N}) \tag{3.2.3}$$

subject to

$$\begin{aligned} &x_{k+1} = f(x_k, u_k) \\ &X_L \leq x_i \leq X_U, \text{ for } 0 \leq i \leq n+j \\ &U_L \leq u_i \leq U_U, \text{ for } 0 \leq i \leq n+j \\ &Y_{L,i} \leq y_i \leq Y_{U,i}, \text{ for } 1 \leq i \leq n+j \end{aligned} \tag{3.2.4}$$

Since the model $f(x_k, u_k)$ is nonlinear, the convex QP problem in 3.2.1 turns into a nonlinear and nonconvex problem. This complicates the solution considerably since it now needs a nonlinear programming solver.

3.2.2 Non-linear Programming

One of the most effective solving techniques for NLP problems is Sequential Quadratic Programming (SQP). SQP divides the problem into several subproblems and then generate steps. By defining a general nonlinear optimisation problem as,

$$\begin{aligned} &\min_x f(x) \\ &\text{s.t.} \quad \begin{aligned} c_e(x) &= 0 \\ c_i(x) &\leq 0 \end{aligned} \end{aligned} \tag{3.2.5}$$

where $f(x)$ is the nonlinear objective function, $c_e(x)$ and $c_i(x)$ is the nonlinear equality and inequality constraints. The SQP approach is to approximate $f(x)$ by,

$$\hat{f}(x) \approx \frac{1}{2} p^\top \nabla^2_{xx} \mathcal{L}(x_k, \lambda_k) p + \nabla f(x_k)^\top p \tag{3.2.6}$$

where $\mathcal{L}(x_k, \lambda_k)$ is the Lagrangian function and p is the direction of the next iterate. One way of finding p is Newton's method. This method is an iterative solution to non-linear algebraic problems. Given the objective function $f(x_k)$ and an initial guess vector x_0, the search is given by (Nocedal and Wright, 2006),

$$p_k^N = -\nabla^2 f(x_k)^{-1} \nabla f(x_k) \tag{3.2.7}$$

If the initial guess is sufficiently close to the solution, the iteration $x_{k+1} = x_k + p_k$ will converge to the solution. Since the Hessian matrix $\nabla^2 f(x_k)$ may not always be positive definite, Newton's method has only local convergence.

Chapter 4

Modelling

This chapter contains the description of how the process is modelled, and what assumptions are made. The model validation and results are presented along with a discussion and the conclusions. As the model is adjusted to fit with the data given by SSAB, values used and specific details are not presented in this thesis. The parts from the preliminary report include Section 4.2.4, 4.3, 4.5, 4.6.1, first part of 4.7 and 4.8. For more details regarding the modelling, the reader is referred to (Dyrdal, 2017).

4.1 Control Volumes

The main phases of the converter can be divided into four: gas, slag, molten metal and solid metal. By dividing the bath into different control volumes, the heterogeneity challenge is handled. In addition to the slag control volume, the bath is divided into centre, bulk and bottom.

The centre control volume includes the jet penetration, oxidising reactions and bath agitation between centre and bulk. The composition of species in the centre differs from the compositions in bulk and bottom. Towards the end of the blow, the concentration of impurities such as carbon is low and is therefore dependent on the agitation and stirring of the bath for full decarburisation. The centre interacts with bulk and slag, which transfer oxides to slag and low carbon metal to bulk, and receives high carbon metal from bulk.

The bottom control volume handles the gas injection from the tuyeres and the mass transfer between the bulk and bottom. The bulk control volume consists of most of the molten metal, scrap melting and includes the slag-metal reactions.

In addition to the bath control volumes, the slag control volume consists of the oxides and deals with flux dissolution and reactions with both centre and bulk. The converter control volumes are presented in Figure 4.1. The control volumes in

the exhaust system is presented in Section 4.7.

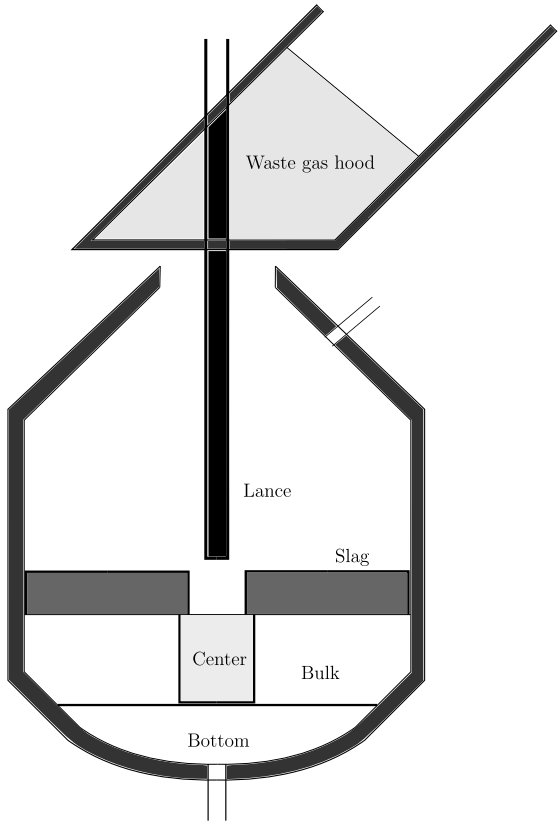

Figure 4.1: Converter with control volumes

4.2 Reactions

In a basic oxygen furnace, there are many reactions between trace elements and oxygen or oxides. The intermediate reactions are not included in this model, neither are the reactions for trace species such as chromium, vanadium and aluminium. This is not entirely correct in chemical terms but is assumed accurate enough to reproduce the process' behaviour. The model includes eleven reactions which occur in three different areas of the process.

(3.3)

1. Impact surface between oxygen jet and centre control volume:

$$[Fe] + \frac{1}{2}O_2(g) \rightarrow (FeO) \tag{r_1}$$
$$[C] + \frac{1}{2}O_2(g) \rightarrow CO(g) \tag{r_2}$$
$$[Si] + O_2(g) \rightarrow (SiO_2) \tag{r_3}$$
$$[Mn] + \frac{1}{2}O_2(g) \rightarrow (MnO) \tag{r_4}$$
$$2[P] + \frac{5}{2}O_2(g) \rightarrow (P_2O_5) \tag{r_5}$$

2. Surface area between bulk and slag control volume:

$$(FeO) + [C] \rightleftharpoons [Fe] + CO(g) \tag{r_6}$$
$$2(FeO) + [Si] \rightleftharpoons 2[Fe] + (SiO_2) \tag{r_7}$$
$$(FeO) + [Mn] \rightleftharpoons [Fe] + (MnO) \tag{r_8}$$
$$5(FeO) + 2[P] \rightleftharpoons 5[Fe] + (P_2O_5) \tag{r_9}$$
$$(Fe_2O_3) + [Fe] \rightleftharpoons 3(FeO) \tag{r_{10}}$$

3. Post combustion modelled in the waste gas hood control volume:

$$CO(g) + \frac{1}{2}O_2(g) \rightarrow CO_2(g) \tag{r_{11}}$$

4.2.1 Decarburisation

The kinetics of the decarburisation is considered to be of high importance. The amount of carbon highly influences the bath's temperature, in addition to impacting the final alloy's properties such as ductility and strength. In the previous model, the activity of carbon was modelled on an approximation of the dilution of carbon in the steel. The activities were modelled as,

$$a_C = \gamma_C^\circ \epsilon_C([\%C])x_C \tag{4.2.2a}$$
$$a_{C_{eq}} = \gamma_C^\circ \epsilon_C([\%C_{eq}])x_{C_{eq}} \tag{4.2.2b}$$

Where ϵ_C is the dilution of carbon. However, due to that the $x_{C_{eq}}$ was set to a fixed value, the equilibrium did not depend on the process. Hence, a new model of the reaction was implemented with this in mind. The new equilibrium as defined in Turkdogan (2000) is,

$$[\%C]_{eq} = \frac{p_{CO}}{a_{FeO}K_6} \tag{4.2.3}$$

where the the partial pressure of CO, p_{CO}, and the equilibrium, K_6, is (Turkdogan, 2010),

$$p_{CO} = p_{CO,0} \frac{r_2 + r_6}{r_2 + r_6 + \epsilon F_{inert}} \tag{4.2.4a}$$

$$\log K_6 = \frac{-5730}{T} + 5.096 \tag{4.2.4b}$$

where $p_{CO,0}$ is the reference pressure of CO in the vessel and ϵ is the dilution of inert gas in the CO bubbles.

Using this the reaction rate for decarburisation between slag and metal is,

$$r_6 = k_6 A e^{\frac{-E_6}{RT}} ([\%C] - [\%C]_{eq}) \tag{4.2.5}$$

where k_6 is the reaction parameter calculated using equation 4.3.2, A is the interaction area between slag and metal. The activity of iron oxide, a_{FeO}, is modelled using the activity coefficients dependency on basicity presented in Figure 2.5.

The bottom stirring is an important process factor for the BOF converter. The bottom stirring in this model is handled by increasing the bottom control volume and adjusting the efficiency of the injected gases, 4.4.8. In Turkdogan (2010) and from the data given by SSAB, the carbon times oxygen factor is a good indication whether the bottom stirring is working or not. With good stirring effect, the factor is 20, and with no or poor stirring the factor averages around 30-40. In Figure 4.2 it is visible that with no bottom stirring it is harder to reach the desired carbon content of, i.e. 0.03%. Under normal process condition, the CO-factor lies in between the two lines of optimal bottom stirring and no bottom stirring. Wear and tear on the bottom tuyeres can affect the efficiency of the stirring, and increase the CO-factor.

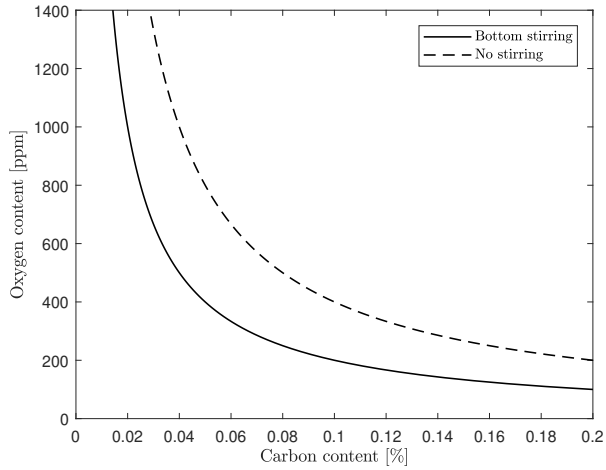

Figure 4.2: Effect of bottom stirring on the oxygen efficiency

4.2.2 Dephosphorisation

The activity of P_2O_5 in slag and the equilibrium of the reaction, r_9, has been investigated in many reports. There are numerous ways of calculating its equilibrium and the reaction rate, and they are all highly dependent on the process, giving very different results. In ordered to compare the obtained reaction rate, it was modelled in two different ways. First by using the activity and the equilibrium coefficient and secondly using phosphorus partition ratio.

For the first method, for lime-based low-P_2O_5 slags the activity of coefficient of P_2O_5 is as presented in Turkdogan (2000),

$$\ln \gamma_{P_2O_5} = -9.84 - 0.142(wt\%CaO + 0.3wt\%MgO) \tag{4.2.6}$$

The equilibrium for the reaction is derived from data in HSC (Roine and al., 2007),

$$\ln K_9 = \frac{216867}{RT} - \frac{197.437}{R} \tag{4.2.7}$$

Using this and assuming the activity of phosphorus is proportional to molar fraction, the reaction rate is then

$$r_9 = k_9 A e^{\frac{-E_9}{RT}} ({x_P}^2 {a_{FeO}}^5 - \frac{{x_{Fe}}^5 a_{P_2O_5}}{K_9}) \tag{4.2.8}$$

For the second method, there are many models trying to approximate the phosphorus partition ratio in steelmaking. These vary for different types of slag and some being temperature dependent. The partition ratio found for the best fit in this process, as presented in (Drain et al., 2016) is,

$$\ln L_p = \frac{22350}{T} + 0.07(wt\%CaO) + 2.5\ln(wt\%FeO) - 16.4 \tag{4.2.9}$$

This leads to a different form for the reaction,

$$r_9 = k_9 A e^{\frac{-E_9}{RT}} ([wt\%P]L_p - (wt\%P)) \tag{4.2.10}$$

where $(wt\%P)$ is the mass percentage of phosphorous as P_2O_5 in the slag phase.

Drain et al. (2016) investigated numerous of different equilibrium constants and partition ratios for different types of slag. The activity coefficients and partition ratios tested are presented in Table 4.1 and 4.2.

Table 4.1: Partition Ratios Phosphorus (Drain et al., 2016)

Equation	Condition	No
$\ln L_p = \frac{22350}{T} + 7\ln(\%CaO) + 2.5\ln(\%Fe_tO) - 24.0$	1580-1669°C	1
$\ln L_p = \frac{22350}{T} + 0.08(\%CaO) + 2.5\ln(\%Fe_tO) - 16.0$	1580-1669°C	2
$\ln L_p = \frac{22350}{T} + 5.6\ln(\%CaO) + 2.5\ln(\%Fe_t) - 21.876$	∼1600°C	3
$\ln L_p = 0.056(\%CaO) + 2.5\ln(\%Fe_t) + 0.5\ln(\%P_2O_5) + 12000/T - 10.42$	∼1600°C	4
$\ln L_p = 3.5\ln(\%CaO) + \frac{4977}{T+17.8} + 2.5\ln(\%FeO) + 0.5\ln(\%P_2O_5) - 10.46$	1550-1650°C	5
$\ln L_p = 2.5\ln(\%Fe_t) + 0.0715(\frac{B}{1+B}(80 - \frac{71.85}{55.85}(\%Fe_t)) - 3.23)$	MgO-MnO, 1000-1680°C	6
$\ln L_p = 0.0680[(\%CaO) + 0.42(\%MgO) + 1.16(\%P_2O_5) + 0.2(\%MnO)] + \frac{11570}{T} - 10.520 + 2.5\ln(\%Fe_t)$	MgO-MnO, 1600-1655 °C	7
$\ln L_p = 0.0157(\%CaO) + \frac{115722.2}{T} - 5.1795 + 0.109\ln(\%Fe_t) - 0.780[C]$		8
$\ln L_p = 0.429B + \frac{13572.2}{T} - 5.329 + 0.0432\ln(\%Fe_t) - 1.009[C]$		9
$\ln L_p = \frac{22350}{T} + 0.07(\%CaO) + 2.5\ln(\%FeO) - 16.4$	Adjusted version of No 2	13

Table 4.2: Activity Coefficients Phosphorus

Equation	Reference	No
$\ln \gamma_{P_2O_5} = 1.01(23N_{CaO} + 17N_{MgO} + 8N_{FeO} - \frac{26300}{T} + 11.2)$	(Turkdogan, 2000)	10
$\ln \gamma_{P_2O_5} = -12.6 - 0.134((\%CaO) + 0.33(\%MgO))$	(Turkdogan, 2000)	11
$\ln \gamma_{P_2O_5} = -1.12(22N_{CaO} + 15N_{MgO} + 13N_{MnO} + 12N_{FeO} - 2N_{SiO_2}) - \frac{42000}{T} + 23.58$	(Basu and Seetharaman, 2007)	12

4.2.3 Iron Oxide Rate

During blowing the operator may add pellets, which is typically used in blast furnaces and contain 60%-75% iron. This is to adjust the chemical composition, adding more iron and oxygen to the bath. As iron oxide, FeO, is unstable at lower temperature, these pellets contain mostly Fe_2O_3. When the pellets are melted into the slag phase, it reacts with the iron in the bath, creating pure iron oxide, FeO.

$$r_{10} = k_{10} A e^{\frac{-E_{10}}{RT}} (x_{Fe_2O_3} x_{Fe} - \frac{{a_{FeO}}^3}{K_{10}}) \tag{4.2.11}$$

where the equilibrium constant is,

$$\ln K_{10} = \frac{-67595 + 84.267T}{RT} \tag{4.2.12a}$$

4.2.4 Other Reaction Rates

Centre Reactions

In the impact area of the oxygen jet, the oxygen enters the bath with supersonic velocity. This rapidly reacts with the species in the bath, creating carbon monoxide and oxides to the slag.

The reactions between oxygen and other species are modelled with respect to the likelihood of an oxygen molecule hitting an atom of another species. These reactions are modelled on the assumption that no reversible reactions occur.

$$\alpha = \sum_{k=1}^{5} \frac{\gamma_k}{\sigma_k} x_i \tag{4.2.13a}$$

$$r_k = \frac{\eta F_{O_2}}{\alpha} \frac{x_i}{\sigma_k} \tag{4.2.13b}$$

where γ_k and σ_k is the stoichiometry coefficients for the oxygen component and the metal component, respectively, in reaction k, where $k = \{1, 2, 3, 4, 5\}$ for the reactions 4.2.1. $F_{O_2}[mol/s]$ is the utilised oxygen flow rate, η is the oxygen utilisation factor and x_i the molar fraction of the metal component, i, in the reaction.

Oxidation of Silicon

The activity of silicon dioxide is dependent on the concentration of the other species in the slag, as presented in the ternary in Figure 2.3. The reaction rate is modelled as,

$$r_7 = k_7 A e^{\frac{-E_7}{RT}} (a_{Si}(a_{FeO})^2 - \frac{a_{SiO_2}(x_{Fe})^2}{K_7}) \tag{4.2.14}$$

where (Ohta and Suito, 1998),

$$\log a_{SiO_2} = 0.036(wt\%MgO) + 0.061(wt\%Al_2O_3) + 0.123(wt\%SiO_2) - \frac{0.595}{B} - 6.456 \tag{4.2.15a}$$

$$\log \gamma^{\circ}_{Si} = -6100/T + 1.21 \tag{4.2.15b}$$

$$\ln K_7 = \frac{437846}{RT} - \frac{82.544}{R} \tag{4.2.15c}$$

Oxidation of Manganese

Assuming that the activity of manganese and iron in the metal is proportional to the molar fraction, the reaction rate is

$$r_8 = k_8 A e^{\frac{-E_8}{RT}} (x_{Mn} a_{FeO} - \frac{x_{Fe} a_{MnO}}{K_8}) \tag{4.2.16}$$

where a_{MnO} is dependent on the basicity and the equilibrium is,

$$K_8 = \frac{(\%MnO)}{(\%FeO)[\%Mn]} \tag{4.2.17a}$$

$$\log K_8 = \frac{7452.0}{T} - 3.478 \tag{4.2.17b}$$

Post-Combustion Rate

In this model it is assumed that there is full post-combustion, that means that all of the carbon monoxide reacts with oxygen to create carbon dioxide. Using this assumption the reaction rate for post-combustion is,

$$r_{11} = r_2 + r_6 \tag{4.2.18}$$

This assumption is also used later for calculating the amount of false air entering the waste gas hood.

4.3 Oxygen Jet

Deo and Boom (1993) presented different methods of calculating the penetration depth, the method used in this model is,

$$dH = L_h \exp\left(-0.04147X^2 + 1.3418X - 8.4297\right) \tag{4.3.1a}$$

where

$$X = \ln(M/L_h^3) \tag{4.3.1b}$$

$$M = 1.421 d_t^2 p_0 [1 - (p_{amb}/p_O)^{0.286}]^{\frac{1}{2}} \tag{4.3.1c}$$

L_h is the lance height relative to the bath, d_t is the throat diameter of the nozzle, p_{amb} is the ambient pressure and p_O is the oxygen pressure.

Using the penetration depth, the reaction constants are (Hammervold, 2010),

$$k_i = a_i + b_i dH \tag{4.3.2}$$

where dH is the penetration depth found in equation 4.3.1 and a_i and b_i is parameters for tuning. i is the reaction index, as listed in 4.2.1.

4.3.1 Emulsion and Metal-slag Interfacial Area

Emulsion

The emulsion height, or foam height, is an important process factor for the operator to avoid slopping. Slopping is the event when the slag foam is forced through the converters mouth. It is a frequent phenomenon in top-blown converters. There has been done some extensive work on predicting the foam height in the converter. A simple model was presented in (Sarkar et al., 2015*b*), but this showed too low foam height and was not dependent on the gas flow. Zhang and Fruehan (1995) presented a model including the gas flow, viscosity and surface tension of the slag. Defined as,

$$h = 115 \frac{\mu^{1.2}}{D_b^{0.9} \rho \sigma^{0.2}} j \tag{4.3.3}$$

where j is the superficial gas flow, D_b is the metal droplet diameter, ρ is density of slag, μ is the viscosity of slag and σ is the surface tension. μ, σ and D_b is adapted from Jung and Fruehan (2000).

Brämming (2010) did a thorough investigation in the predicting the foam height. He found that the vessel vibrations had good correlation with the foam height. Since neither vessel vibration or off-gas measurements (except temperature) are available, the emulsion height in this model is modelled as in equation 4.3.3.

Metal-slag Interfacial Area

For the reaction between the slag and bulk phase, the interfacial area is dependent on both the geometric area, but also the number of metal droplets in the slag phase. This can be modelled as (Subagyo et al., 2003)(Turkdogan, 2010),

$$A = A_{bulk,slag} + x_{droplet} \frac{V_{slag}}{d_{droplet}} \tag{4.3.4}$$

$x_{droplet}$ is the fraction of metal droplets in slag, and $d_{droplet}$ is the diameter of the metal droplets. These values are set to fixed values, $x_{droplet} = 0.05$ and $d_{droplet} = 3mm$.

In addition, it is expected that the interfacial area is also dependent on the bottom stirring. Higher stirring effect will lead to more oxides, FeO in particular,

circulate the bulk phase and react with the trace species in the metal. Hence, increasing the reaction rate. Including the metal droplets in slag, the area is,

$$A = A_{bulk,slag} + x_{droplet}\frac{V_{slag}}{d_{droplet}} + x_{oxide}\frac{w_b \tau}{\rho d_{oxide}} \tag{4.3.5}$$

Where τ is a time constant for the residence time of oxides in the metal bath.

4.4 Mass Transfer

Using the equation 2.4.3 in Section 2.4 and assuming the density is constant through the control volume the equation simplifies to

$$\frac{dm}{dt} = \dot{m} = -\iint \rho v^\top n \, dA \tag{4.4.1}$$

Then the mass balance for each species in the control volume is

$$\dot{m}_i = w_{i,in} - w_{i,out} \tag{4.4.2}$$

where i represents the species in the control volume and w_{in} and w_{out} is the mass transfer in and out of control volume, respectively. Figure 4.3 illustrates the mass transfers between the bath control volumes.

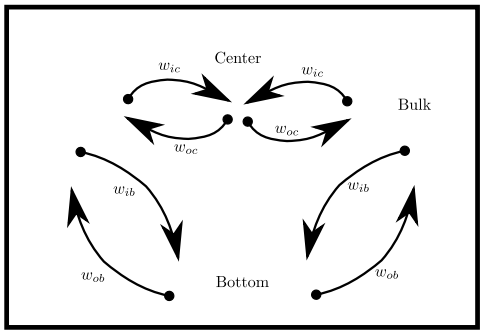

Figure 4.3: Resulting mass transfer from agitation and stirring

The mass balance for the bulk control volume includes the scrap melting, stirring from centre and bottom and the reactions with the slag phase.

$$\dot{m}_{Fe} = w_{Fe,in} - w_{Fe,out} + M_{Fe}(r_6 + 2r_7 + r_8 + 5r_9 - r_{10}) + x_{Fe}w_{melt} \tag{4.4.3a}$$

$$\dot{m}_C = w_{C,in} - w_{C,out} - M_C r_6 + x_C w_{melt} \tag{4.4.3b}$$

$$\dot{m}_{Si} = w_{Si,in} - w_{Si,out} - M_{Si} r_7 + x_{Si} w_{melt} \tag{4.4.3c}$$

$$\dot{m}_{Mn} = w_{Mn,in} - w_{Mn,out} - M_{Mn} r_8 + x_{Mn} w_{melt} \tag{4.4.3d}$$

$$\dot{m}_P = w_{P,in} - w_{P,out} - 2M_P r_9 + x_P w_{melt} \tag{4.4.3e}$$

For the slag phase, the mass balance includes the dissolution of fluxes in addition to the reactions.

$$\dot{m}_{FeO} = M_{FeO}(r_1 - r_6 - 2r_7 - r_8 - 5r_9 + 3r_{10}) + x_{FeO}w_{dissolution} \tag{4.4.4a}$$

$$\dot{m}_{SiO_2} = M_{SiO_2}(r_3 + r_6) + x_{SiO_2}w_{dissolution} \tag{4.4.4b}$$

$$\dot{m}_{MnO} = M_{MnO}(r_4 + r_8) \tag{4.4.4c}$$

$$\dot{m}_{P_2O_5} = M_{P_2O_5}(r_5 + r_9) \tag{4.4.4d}$$

$$\dot{m}_{CaO} = x_{CaO}w_{dissolution} \tag{4.4.4e}$$

$$\dot{m}_{MgO} = x_{MgO}w_{dissolution} \tag{4.4.4f}$$

$$\dot{m}_{Fe_2O3} = M_{Fe_2O_3}(-r_{10}) + x_{Fe_2O_3}w_{dissolution} \tag{4.4.4g}$$

$w_{dissolution}$ is the dissolution rate of additive materials and x_i is the molar fraction.

Only the centre reactions and the stirring affect the mass transfer for the centre control volume. Hence, the mass transfer can be summarised as,

$$\dot{m}_i = w_{i,in} - w_{i,out} - M_i\sigma_k r_k \tag{4.4.5}$$

where σ_k is the stoichiometry coefficients for the metal component in reaction r_k for $k = 1, 2, 3, 4, 5$. The molar masses used in the model are presented in Table 4.3

Table 4.3: Molar masses in $[g/mol]$ for selected species (Roine and al., 2007)

Species	Fe	C	Si	Mn	P	FeO	SiO_2	MnO	P_2O_5	CaO	MgO	Fe_2O_3
Molar mass	55.85	12.01	28.09	54.94	30.97	71.85	60.08	70.94	141.94	56.08	40.30	159.69
Gas species	O_2	CO	CO_2	N_2	Ar							
Molar mass	32	28.01	44.01	28.01	39.95							

For the bottom phase, only argon or nitrogen are blown, and therefore the only mass transfer is from stirring. The mass transfer between bottom and bulk, in kg/s resulting from bottom blowing, were calculated by using the formulas presented in (Naito et al., 2002).

$$w_b = \ln\left(\frac{1}{1 - 0.95}\right)\frac{m_{tot}}{t_b} \tag{4.4.6}$$

where the stirring time, $t_b[s]$, is

$$t_b = 100\left[\frac{(\frac{D^2}{H})^2}{e_b}\right]^{0.337} \tag{4.4.7}$$

where $D[m]$ is the vessels diameter, $H[m]$ is the bath depth and $e_b[J]$ is the bottom stirring energy, defined as

$$e_b = \eta_b\frac{6.18QT}{W}\left[\ln(1 + \frac{9.8\rho H}{P_{atm}}) + 0.06\left(1 - \frac{T_{O_2}}{T_{steel}}\right)\right] \tag{4.4.8}$$

Where η_b is defined as the bottom stirring efficiency. The bottom stirring has a tremendous effect on the decarburisation of the molten metal, and the value

of this parameter is expected to vary in time due to wear on bottom tuyeres. In reality, the converter has several tuyeres where each tuyere can be clogged or partly clogged. As there is no data on this, the stirring efficiency parameter is expected to reproduce same results.

4.5 Dissolution of Additions and Scrap Melting

To achieve the desired composition and temperature of the steel bath, it is often necessary to add certain additions. These additions may have big influences on the slag behaviour or the molten bath behaviour. Adding scrap to the molten bath does not only decrease costs, but it also increases the content of iron and cools the bath. The addition of fluxes as lime and pellets gives the operator the possibility to alter the kinetics and temperature of the slag.

Melting of scrap is a dissolution phenomenon where both heat transfer and mass transfer between solid and liquid phase takes place. Carbon governs the mass transfer between the two phases if the carbon content of the liquid phase is much higher than in the solid phase, the absorption of carbon from liquid to solid decreases the melting temperature of solid phase (Li and Provatas, 2008). In addition, the added scrap, in general, has much lower temperature than the bath. Hence, there forms a solidified layer around the scrap. This layer and the additives is then melted and diffused into the liquid phase. Both of these phenomena affect the total melting time of the addition.

For the dissolution of solid oxides in the slag phase, it is dependent on the slag composition, temperature of the slag phase and the mixing between metal and slag phase (Dogan et al., 2009).

The melting and dissolution mechanism vary for the different types of additions. Here important factors are the melting temperature of the addition, grain size and solubility of the additives. For simplification, the generation of a solid layer around the addition material and the difference in carbon content is ignored. Hence the melting rate and dissolution rate can be simplified to these equations

$$\frac{dR}{dt} \approx \frac{k_{htc}(T - T_m)}{\rho(\Delta h_L + C(T - T_0))} \tag{4.5.1}$$

where Δh_L and k_{htc} are the latent heat and heat transfer coefficient, respectively. T_m and T_0 are the melting temperature and loading temperature of the addition.

The dissolution rate of lime is assumed to be dependent on the liquidus temperature of lime, while the dissolution rate of dolomite is expressed in terms of the saturation of MgO,

$$w_{lime,dissolution} = \frac{m_{slag}}{10} K_{lime}(T_{slag} - T_{liq}) \tag{4.5.2a}$$

$$w_{dolo,dissolution} = \frac{m_{slag}}{10} K_{dolo}(MgO_{sat} - x_{MgO}) \tag{4.5.2b}$$

where K_i is the activity coefficient, T_{liq} is the liquidus temperature and x_{MgO} is the molar fraction of MgO in slag.

The liquidus temperature of the slag is calculated using the equation presented in (Seetharaman et al., 2014)

$$T_{liq} = 958{+}656.9x_{SiO2}{+}1440.7x_{CaO}{+}1091x_{MgO}{+}761x_{MnO}{+}522x_{FeO}{+}794x_{Fe_2O_3} \tag{4.5.3}$$

where T_{liq} is the liquidus temperature in Kelvin and x_i is the weight fraction of the species. This has further been refined in order fit the phase diagram presented in Figure 2.3 with the simulated process data during this work.

$$T_{liq} = 1131{+}565x_{SiO2}{+}1110.7x_{CaO}{+}1091x_{MgO}{+}761x_{MnO}{+}422x_{FeO}{+}794x_{Fe_2O_3} \tag{4.5.4}$$

With the slag composition ranging from 0% CaO to 70%CaO it is difficult to create one equation with good accuracy for all the phase fields. The equation has also been averaged to fit the measured data given by SSAB.

Without knowing more about the additives with respect to their size and shapes, this is assumed to be a valid modelling of the rates. As the additives used in the process vary in shapes and size, it makes it hard in practice to take these factors into account.

4.6 Heat Transfer

The majority of the heat transfers in the bath is due to radiation or conduction before the slag phase is created the bulk and centre control volume has a large surface area. During this, both the bulk and the centre loose heat to the surroundings in the form of radiation, when the slag phase is formed the radiation from the bulk phase is practically zero. This is modelled by using Equation 2.6.2.

$$q_{rad} = \sigma_R \epsilon_S A_i (T_i^4 - T_{ref}^4) \tag{4.6.1}$$

Where A_i is the surface area of the control volumes, the surface area for radiation is calculated using the area of the converters mouth, such that the area of the centre is

$$A_{rad,centre} = \frac{h_{bath}}{h_{centre}} cmr A_{mouth} \tag{4.6.2}$$

Where cmr is the ratio between centre control volume mass and the total mass of metal. h is the height of the bath and centre. The slag area is found by taking the minimum of the cross-sectional area and slag area based on a minimum height of 2 cm.

The heat transfer between the phases is due to conduction, and is calculated by Equation 2.6.3.

For heat transfer with both convection and conduction, or through different materials, one needs an averaged heat transfer coefficient. This can be calculated as,

$$k_{ave} = \frac{2k_1k_2}{k_1x_1 + k_2x_2} \tag{4.6.3}$$

Where k_i is the heat transfer coefficient or the thermal conductivity of the material, x_i is the distance. For N transitions and $N+1$ temperatures, the heat transfer can be generalised to

$$Q = \frac{T_1 - T_{N+1}}{\sum_{i=1}^{N} R_i} \tag{4.6.4}$$

where

$$R_i = \begin{cases} \frac{x_i}{k_i A}, \text{conduction} \\ \frac{1}{h_i A}, \text{convection} \end{cases} \tag{4.6.5}$$

4.6.1 Reaction Heat

The heat of reaction is the amount of heat needed to be added or withdrawn to keep the products at the same temperature as the reactants. Assuming the pressure in the vessel is constant, this reaction heat can be calculated using enthalpy. The heat of reaction is then either endothermic or exothermic, most of the net reactions occurring in a steel process are exothermic. When oxygen reacts with the species in the bath energy is released and the temperature of the bath increases. Figure 4.4 presents the difference in energy between the reactants A and B to the product C.

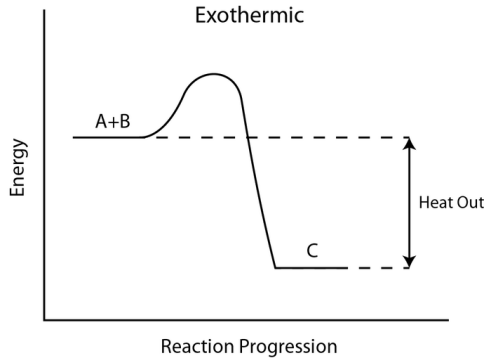

Figure 4.4: Exothermic reaction

Note the increase in energy before the decrease, this comes from the heating of reactants. Hence, the total heat of reaction can be calculating summing the heat added to the reactants and the difference in energy between the product and reactants, as formulated in (Deo and Boom, 1993).

$$\Delta H_T^{\circ,react} = \Delta H_{298}^{\circ,react} + (H_{T_2}^{\circ} + H_{T_1}^{\circ})_{products} - (H_{T_2}^{\circ} + H_{T_1}^{\circ})_{reactants} \tag{4.6.6}$$

Where $\Delta H_{298}^{o,react}$ is the heat of reaction when the products and reactants are in their standard state at 298 K. By assuming that the reactions occur at the average temperature in their respective control volume, the heat of reactions is included in the formulated energy balance.

4.6.2 Heating of Converter Walls

In order to make the simulation of the process continuous, temperature monitoring of the converter lining is added. During blowing heat transfers from the different phases to the lining, hence the there is a difference from a batch with a cold converter to a batch with a warm converter. The lining of the converter consists of different materials. It is mainly divided into three different parts, working lining, safety lining and a steel cape. To make the temperature profile in the lining accurate, several temperatures are included in the lining. The first is at the surface of the working lining and will be at approximately the same temperature as the bath. The next is at 10%, and 30% in the working lining, 80% in the safety lining and the last is at the steel cape. The temperature profile is presented in Figure 4.5.

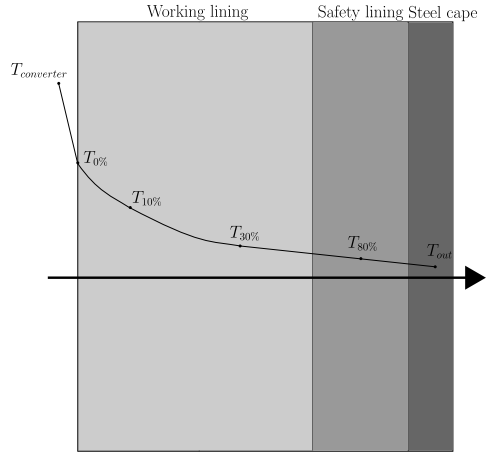

Figure 4.5: Temperatures in the converters lining

The last two temperatures remain nearly constant through the batches, while the first three vary highly with the temperature of the bath and slag.

4.7 Fume

The exhaust system is divided into several sections. The first part is the lower part of the waste gas hood, placed directly above the mouth of the converter. Here the gas from the process together with some false air from the surroundings is sucked in by the exhaust system. The remaining oxygen from the bath reactions and the oxygen from the false air reacts with the carbon monoxide to create carbon dioxide, this is known as post-combustion. The gas is then cooled in the remaining waste gas hood before it gets further cooled in the exhaust system, after cooling the gas enters a scrubber for cleaning.
In the steel refining process there is a limited amount of data during the blowing period, but by measuring the exhaust temperature and the cooling effect in the exhaust system, it is possible to withdraw information about the systems states.

From measuring the fume temperature in addition to the cooling effect, information about the reactions and temperature can be withdrawn and can indicate the composition of the bath.

4.7.1 Fume Composition

The exhaust system is modelled in mol/s, and it is assumed that full combustion takes place, as given from SSAB. In order to calculate the temperature change and the composition of the gas in the exhaust, it is necessary to find the amount of false air that is sucked into the exhaust system. With the assumption of full combustion, this can be calculated by

$$\dot{F}_i = F_{i,in} - F_{i,out} \tag{4.7.1}$$

where

$$F_{i,in} = F_{i,wastegas} + F_{i,air} \tag{4.7.2}$$

An illustration of the energy and gas flow is presented in Figure 4.6.

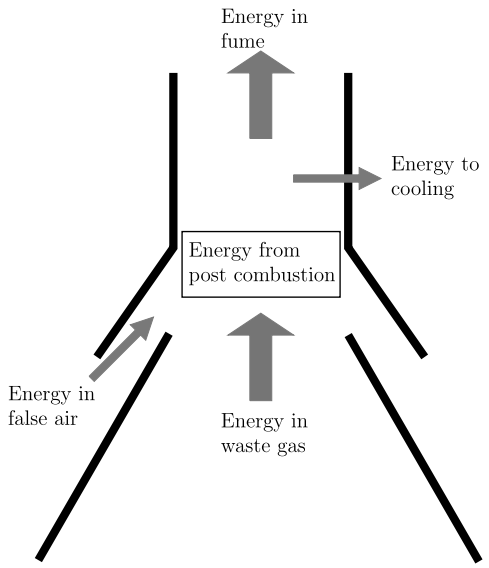

Figure 4.6: Energy flow in waste gas hood

For each species the gas flow is

$$F_{CO,wastegas} = r_2 + r_6 \tag{4.7.3a}$$
$$F_{O_2,wastegas} = (1-\eta)F_{O_2,injection} \tag{4.7.3b}$$
$$F_{CO_2,wastegas} = 0 \tag{4.7.3c}$$
$$F_{N_2,wastegas} = F_{N_2,stirring} \tag{4.7.3d}$$
$$F_{Ar,wastegas} = F_{Ar,stirring} \tag{4.7.3e}$$

$F_{i,air}$ is dependent on the needed oxygen for full combustion, η is the oxygen utilisation of the metal bath. The injection and stirring flows are all inputs to the model. The flow out of the control volume, $F_{i,out}$, is dependent on how fast the fume flow is. Knowing the exhaust flow makes it possible to find the flow out of the volume and hence the flow of fresh air. The fume flow consists of $CO(g)$, $CO_2(g)$, $O_2(g)$, $N_2(g)$ and $Ar(g)$.

As only $CO(g)$, $CO_2(g)$ and $O_2(g)$ take part in the post combustion the mol balance of the waste gas hood becomes:

$$\dot{F}_{CO} = r_2 + r_6 \tag{4.7.4a}$$

$$\dot{F}_{O_2} = \frac{1}{2} r_{11} \tag{4.7.4b}$$

$$\dot{F}_{CO_2} = -r_{11} \tag{4.7.4c}$$

$$\dot{F}_{N_2} = 0 \tag{4.7.4d}$$

$$\dot{F}_{Ar} = 0 \tag{4.7.4e}$$

4.7.2 Cooling Effect

The exhaust system is divided into three different control volumes, the hood above the converter where it is assumed that the post-combustion occurs, the upper part of the waste gas hood with cooling and the exhaust system with cooling.

Before the exhaust gas from the process enters the cleaning system, it is cooled down by a parallel flow of water. In this u-shaped cooling stack, as illustrated in Figure 4.7, the cooling water first enters the upper part of the waste gas hood before entering the cooling stack. The output flow is then measured in terms of mass flow, temperature and the heat power generated.

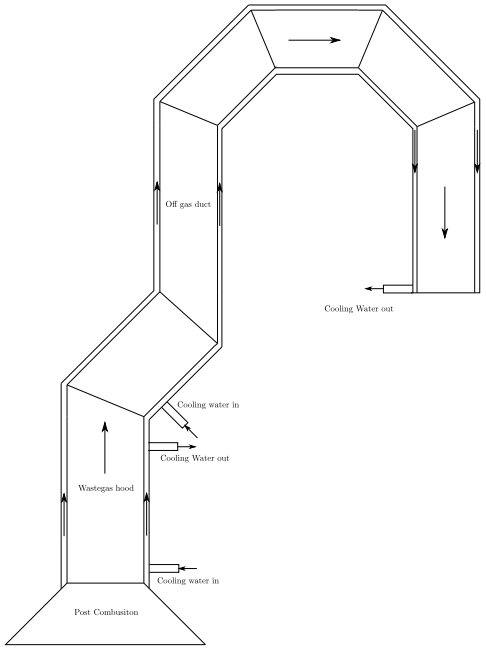

Figure 4.7: Exhaust cooling system

In order to simplify the calculations of the cooling effect, logarithmic mean temperature difference is used instead of partial differential in the Cartesian coordinate system. The logarithmic mean temperature difference for a co-current flow is defined as,

$$T_{LMTD} = \frac{(T_{h,in} - T_{c,in}) - (T_{h,out} - T_{c_o ut})}{\ln(T_{h,in} - T_{c,in}) - \ln(T_{h,out} - T_{c_o ut})} \tag{4.7.5}$$

Where T_h and T_c denote hot and cold side. Using LMTD, the heat from convective heat transfer can be written as,

$$Q_c = h_c A T_{LMTD} \tag{4.7.6}$$

where h_c is the heat transfer coefficient, and A is the surface area. The heat transfer coefficient depends on space, time, geometry, fluid properties and orientation of the surface relative to the flow.

Since the fume temperature and cooling temperature did not correspond well to the measurements in the previous model (Dyrdal, 2017), some adjustments are made to slow down the system. The previous model was modelled with no material between the warm fume and the cooling water. By adding a thin layer of metal, the cooling system is more accurate and slows down the temperature increase in both the off gas and the cooling water. This is modelled as presented in Figure 4.8.

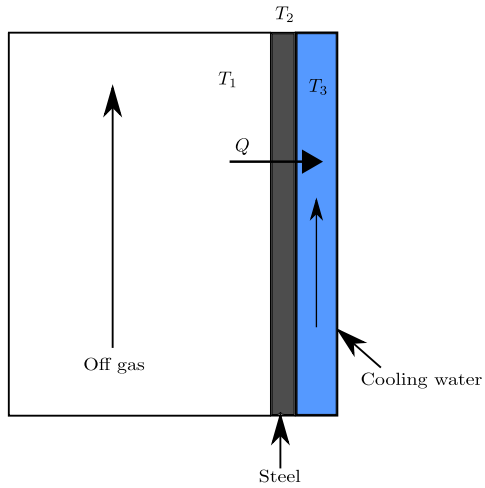

Figure 4.8: Heat from fume to cooling water

By assuming that the kinetic and potential energy of the water flow at the output is equal to the input, we can describe the temperature change in water using energy balance as,

$$\dot{T} = \frac{\dot{m}(h(T_{in}) - h(T_{out})) + Q_c}{mC_p} \tag{4.7.7}$$

4.8 Energy balance

By assuming that the kinetic and potential energy for the system is negligible and density is constant through the control volume, the energy balance becomes

$$\frac{d}{dt}(m(h(T) + \frac{p}{\rho})) + \sum \omega_i(h_i(T_i)) = Q - W_s \tag{4.8.1}$$

Index i being the species present and w_i is the mass flow crossing the control volume surface, defined positive outwards. Since no work is done on the system

$$\frac{d}{dt}(m(h(T) + \frac{p}{\rho})) + \sum \omega_i(h_i(T_i)) = Q \tag{4.8.2}$$

The fraction between pressure and density becomes relatively small compared to the specific enthalpy, since the density of metal is large. Using the same values as in Section 2.5

$$\frac{p}{\rho} = \frac{101325Pa}{3500kg/m^3} = 28.95kJ/kg$$

compared to the specific enthalpy $1023.15\frac{kJ}{kg}$ at 1500℃ of iron. Hence, the expression becomes

$$\frac{d}{dt}(mh(T)) + \sum \omega_i(h_i(T_i)) = Q \tag{4.8.3}$$

By assuming the change in enthalpy is dominated by the change of temperature

$$\frac{d}{dt}(mh(T)) \approx \dot{m}h(T) + m\frac{\partial H}{\partial T}\frac{dT}{dt} \tag{4.8.4}$$

By differentiating the specific enthalpy with respect to temperature, yields the specific heat capacity.

$$\frac{d}{dT}H_i(T) = C_{p,i} \tag{4.8.5}$$

The energy balance then becomes

$$\sum \dot{m}_i h_i(T) + \dot{T}\sum m_i C_{p,i} + \sum w_i(h_i(T_i)) = Q \tag{4.8.6}$$

by re-arranging the energy balance, the temperature change is derived

$$\dot{T} = \frac{Q + \sum (w_{i,in}h_i(T_{in}) - w_{i,out}h_i(T)) - \sum \dot{m}_i h_i(T)}{\sum m_i C_{p,i}} \tag{4.8.7}$$

4.8.1 Consistency Check

To verify that the mass balance and energy balance are correctly implemented, a consistency check is added to the model. The mass balance check for each species in the converter can be summarised as,

$$\dot{m}_i = m_i + \frac{M_i}{M_j}x_j w_{additives} + x_i w_{scrap} \tag{4.8.8}$$

where i is the metal species and j is an oxide.
An enthalpy check was created for both the converter and the off gas system. This is modelled for the converter as,

$$0 = H_{in} - H_{out} - (\Delta H_{centre} + \Delta H_{bulk} + \Delta H_{bottom} + \Delta H_{slag}) \tag{4.8.9}$$

The energy check is modelled as,

$$0 = E_t - E_0 - \int_0^t \dot{E}dt \tag{4.8.10}$$

This also makes it possible to verify that the thermodynamic library and the data written into it is correct.

4.9 Results

The model results presented are simulated using SSAB's process data. SSAB has provided data for many batches with inputs, measurements and initialisation. This facilitated the model validation and made it possible to check whether the assumptions made in the modelling were realistic. However, due to the harsh environment of the BOF process, there is a lack of measurements during blowing, and the correctness of the inputs and measurements are uncertain. Since the data provided by SSAB are confidential, no charge specification or input data is presented, neither are the values for the parameters found. The time axis is defined as from 0 to 100%, denoting start and end of blow respectively.

In this section, the results from the modelling and the validation against process data is presented. Cybernetica's model adjustment and simulation tool, Modelfit, enabled for simulation of the model. With Modelfit the user can easily change the initial states and parameters, add their own inputs to the system or add datasets containing charge specification, measurements and inputs. The main parameters were roughly tuned by using the parameter optimisation in Modelfit, trial and error further adjusted the parameters for the reaction rates and oxygen utilisation. The results have been validated against 14 batches with different initialisation and additions, only some of these batches included slag measurements. Results that have not changed from the preliminary project thesis is included in Appendix A.

4.9.1 Validation

Bath and Slag Temperature

The converter, centre- and slag control volume's temperature is presented in Figure 4.9. These temperatures are highly dependent on the additions and their melting- or dissolution rates, in addition to the exothermic or endothermic heat from reactions.

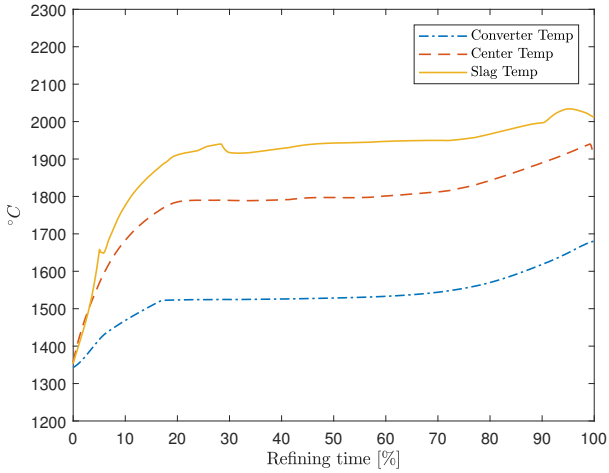

Figure 4.9: Converter, centre and slag temperature during a batch

Metal and Slag Composition

The composition of trace species in the metal and slag during the course of blowing is presented in Figure 4.10. Due to the equilibrium modelling of the slag reactions the content of these species are highly correlated. The species presented for metal are C, Si, Mn and P, for slag the species are FeO, SiO_2, MnO, P_2O_5, CaO, MgO and Fe_2O_3.

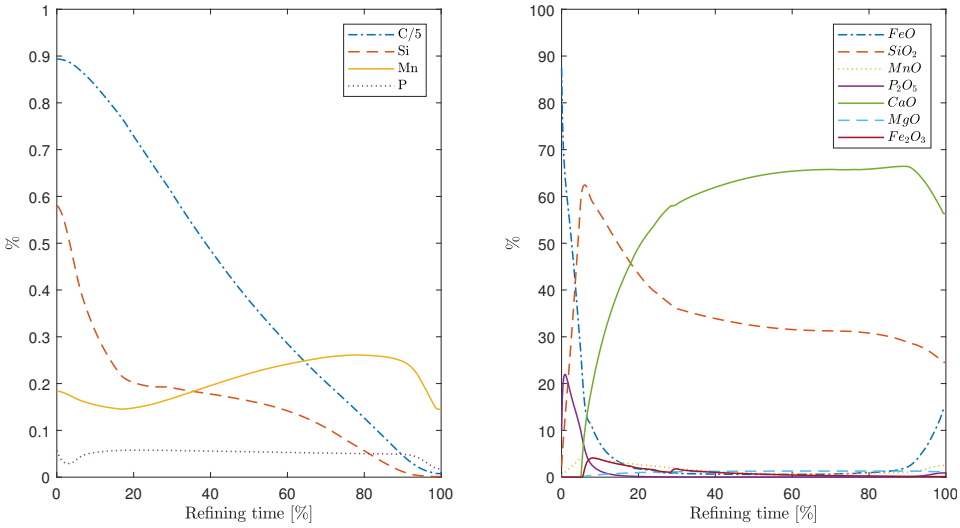

Figure 4.10: Content of species and oxides in metal and slag during blowing

Slag Reactions

The slag reactions are presented in Figure 4.11. The reactions presented are r_6, r_7, r_8, r_9, r_{10} and r_{11}. Since all of these reactions reacts with iron oxide, these are as expected highly dependent on the iron oxide content in the slag.

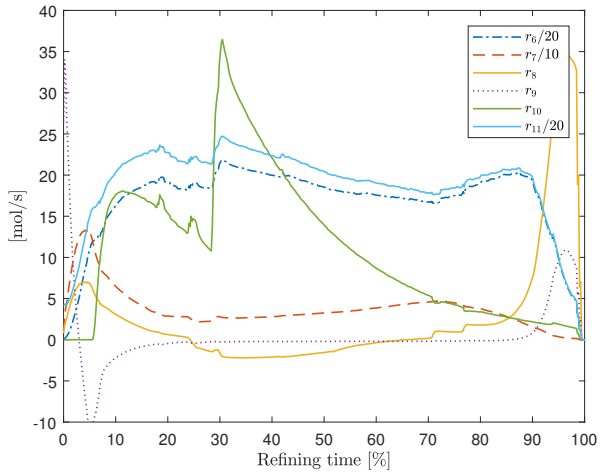

Figure 4.11: Slag reactions

Off Gas Results

The comparison of simulated- (T_{fume}) and measured (T_{meas}) fume temperature together with the correlation is presented in Figure 4.12. In Figure 4.13 the simulated temperature profile of waste gas hood and off gas cooling water is presented against the measurement. Here $T_{c,wgh}$ is the waste gas hoods cooling water temperature and $T_{c,fume}$ is the off gas cooling water temperature.

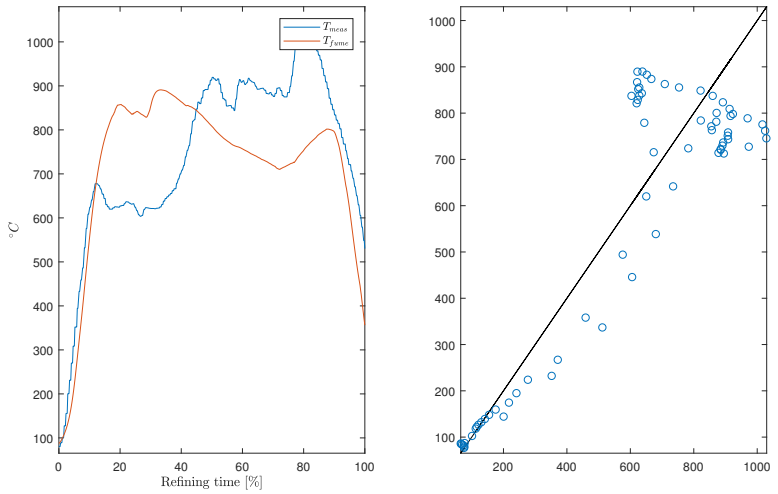

Figure 4.12: The simulated fume temperature against the measured temperature

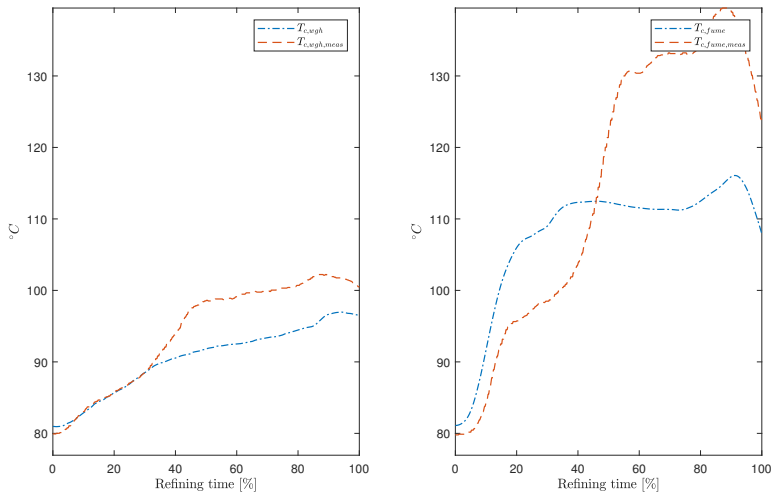

Figure 4.13: Simulated versus measured fume temperature

Carbon and Temperature Error

The difference in simulated and measured carbon content and temperature for 14 different batches is presented in Figure 4.14. This clearly shows the correlation between carbon content and the bath's temperature.

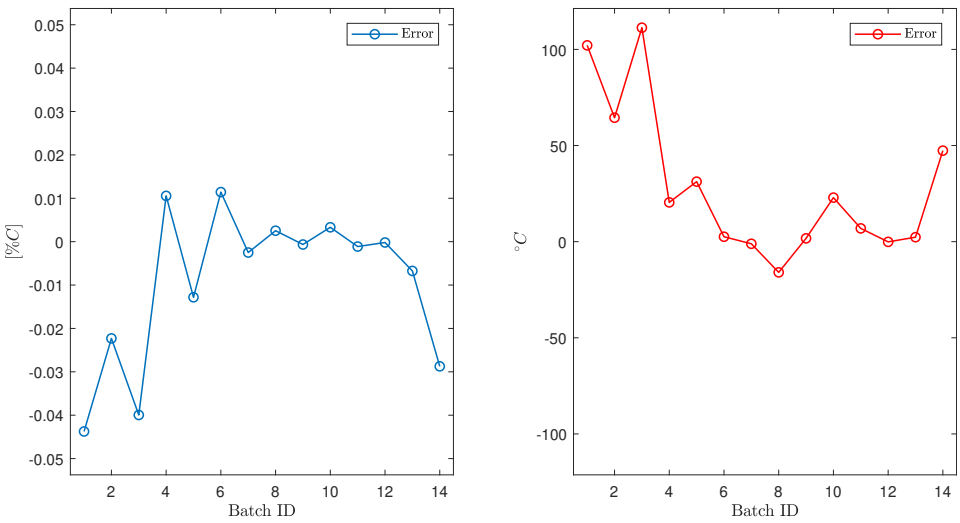

Figure 4.14: Difference in simulated and measured carbon content and temperature for 14 batches

4.9.2 Phosphorus Equilibria

For the phosphorus equilibria presented in Table 4.1 and 4.2 some of them gave promising results. The reaction rates for selected partition ratios is presented in Figure 4.15 for two different batches. Batch number "1" has iron oxide additions, while number "2" has FeSi additions. The different partition ratios have different reaction constants to keep the process stable. The value of the partition ratios in these reaction rates is presented in Appendix A.

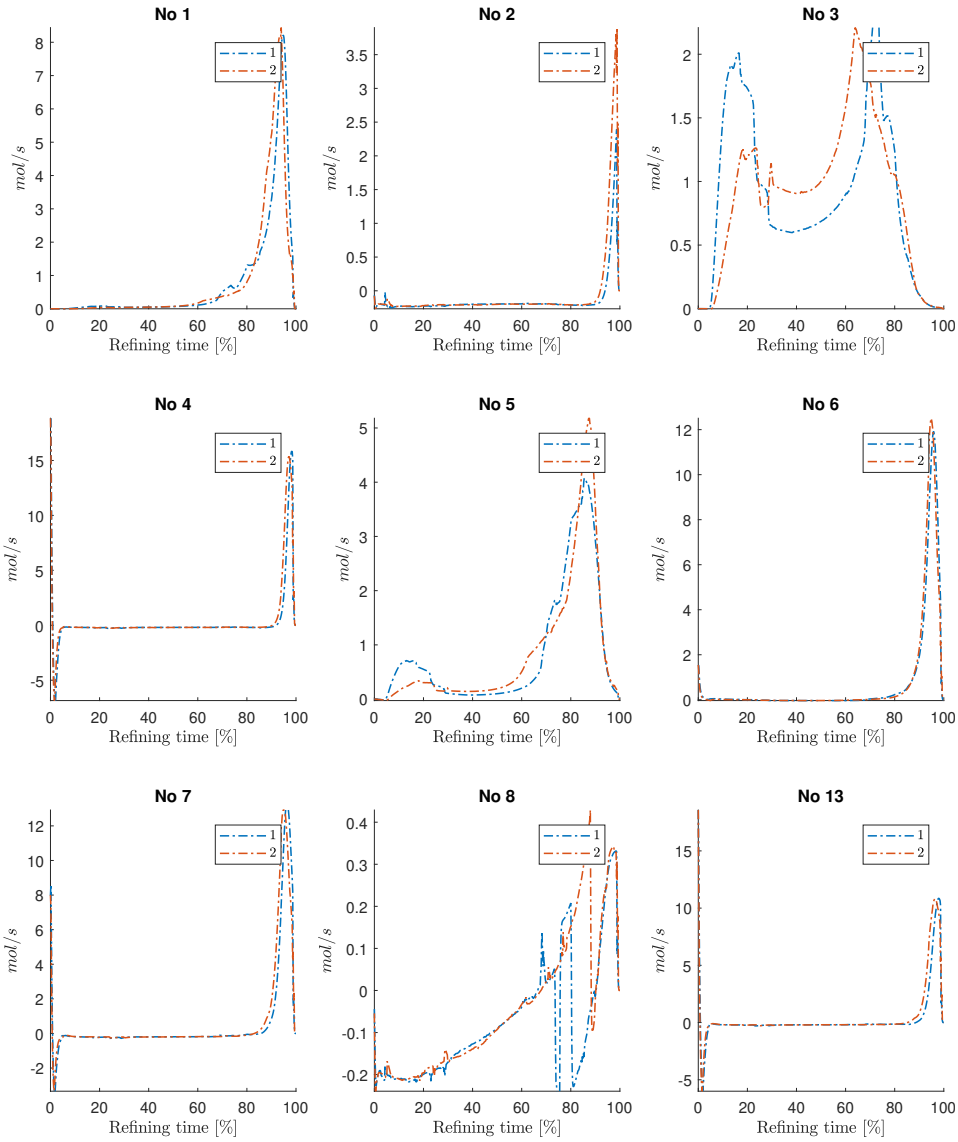

Figure 4.15: Reaction rates for selected phosphorus equilibria for two batches, Table 4.1

4.9.3 Emulsion Height

The emulsion height of a batch is presented in Figure 4.16. The y-axis represents the height of the emulsion layer in meters.

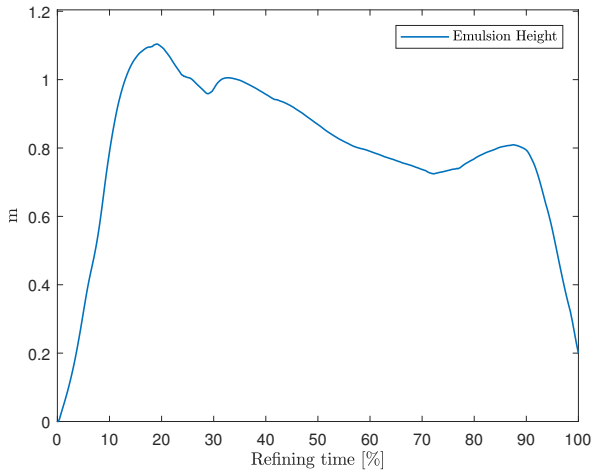

Figure 4.16: Emulsion height during blowing

4.9.4 Lining Temperature

The different temperatures in the lining is presented in Figure 4.17. The temperatures presented are $T_{0\%}$, $T_{10\%}$, $T_{30\%}$, $T_{80\%}$, T_{out} as according to Figure 4.5.

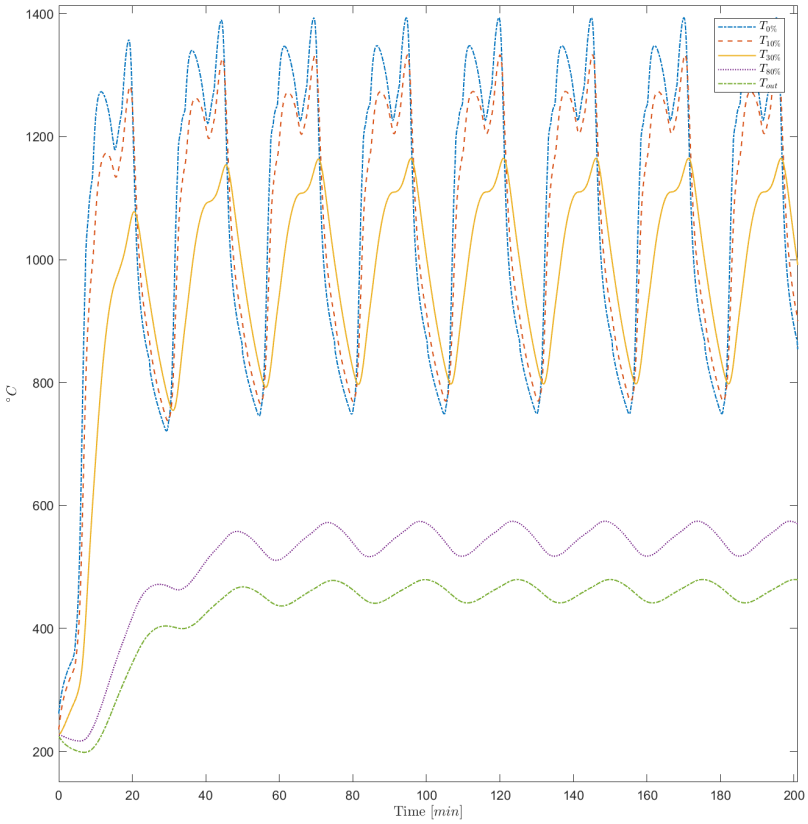

Figure 4.17: Continuous temperature profile in the converters lining

4.10 Discussion

4.10.1 Model Validation

The goal of the modelling was to create a model which correlated well with the measurements given by SSAB and the behaviour that is recommended in literature and could further be used with an estimator and a controller. With the infrequent and few available measurements in the BOF process, a well-correlated model is beneficial in estimating the process' states. There are different measures to validate the model. The main focuses were the bath's temperature, carbon- and phosphorus content. For measurements regarding the bath's composition and temperature, there are no measurements during the heat, the same applies to the slag phase. However, as mentioned earlier, the fume temperature and the cooling systems temperatures are measured during the heat. By using these measurements, one could get a good indicator of whether the reaction kinetics (in particular the CO reactions) in the model is correlated with the real process.

A typical metal and slag content profile is presented in Turkdogan (2010),

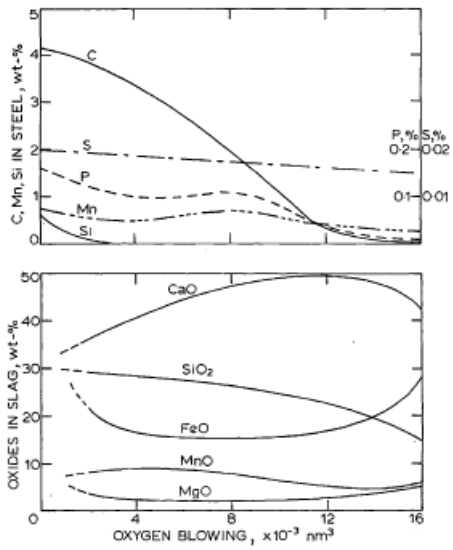

Figure 4.18: BOF trace specie and slag profile, adapted from Turkdogan (2010)

Temperature Profiles

The end temperature of the bath correlated well with the measurements given by SSAB. Comparing the carbon content and the temperature against the measurements, the temperature of the bath is behaving as it should. Higher carbon content than measured yields a lower temperature than measured, and lower carbon content yields a higher temperature. This is in line with the thermodynamics of the

process, as the main producer of heat is the decarburisation.
The bath's temperature profile is naturally affected by the scrap melting. When the bath's temperature reaches the melting temperature of scrap, the temperature increase nearly stops until most of the scrap is dissolved into the molten metal before it increases. Comparing the bath's temperature profile with literature and models presented by Kruskopf and Visuri (2017), it should, however, keep a more linear profile. This may be solved by changing the melting kinetics of scrap to a more advanced model, taking into account an increasing temperature of the scrap. As it is modelled now, Equation 4.5.1, the temperature of the scrap remains constant at ambient temperature. This causes the scrap to draw more energy in the start before it heats up and dissolves into the metal.

Metal and Slag Composition

For the metal composition, the silicon content does not decrease as rapidly as suggested in Turkdogan (2010). This is a consequence of the low level of iron oxide in the slag. However, the profile fits well with other models presented in literature, such as Kruskopf and Visuri (2017) and Sarkar et al. (2015*a*). Here the silicon content decreases quickly the first 20% before remaining about constant towards 80% of the blowing time.

Figure 4.14 presented the carbon and temperature error for 14 different batches. These results show high deviations from the measured results for the three first batches and the last batch. Discussing these batches with SSAB, it showed that for the first batch, the bottom stirring was almost non-existing, requiring a much longer blowing time. For the other batches, the source of the error is unknown. To have full faith in the measurements, more information about the process and the measurements from the heat is required.

The iron oxide content in the slag is lower than what is expected, but the end-point content fits well with the few measurements given on the slag content. Comparing the profiles of CaO, SiO_2 and FeO with Figure 4.18, Kruskopf and Visuri (2017) and Sarkar et al. (2015*a*). The profiles match well with Figure 4.18 and the results presented in Sarkar et al. (2015*a*), with a slowly decreasing SiO_2 content due to the decreasing amount of Si in the metal, low FeO content in the slag until the carbon content approaches its equilibrium and high CaO content from the added lime. However, it does not match well with the results presented in Kruskopf and Visuri (2017) and the model compared against in the report. It is hard to say which one is more accurate for this process without having measurements of the slag content during blowing. The slag weight after the heat would also be a good indicator of which is correct.

Reaction Kinetics

The centre reaction rates are modelled the same way as in the preliminary report and are presented in Appendix A.

The reaction kinetics between iron oxide and carbon is modelled with the equilibrium depending on the partial pressure of CO-bubbles, activity of iron oxide and the equilibrium constant. In Figure 4.19 the equilibrium, and measured data for BOP and Q-BOP are presented as in Turkdogan (2010) together with the simulated results from the model. The low iron oxide content in the model's slag is evident here as well, to the match the measured carbon content, the equilibrium is adjusted down. However, at higher iron oxide content, it correlates well with the measured Q-BOP results.

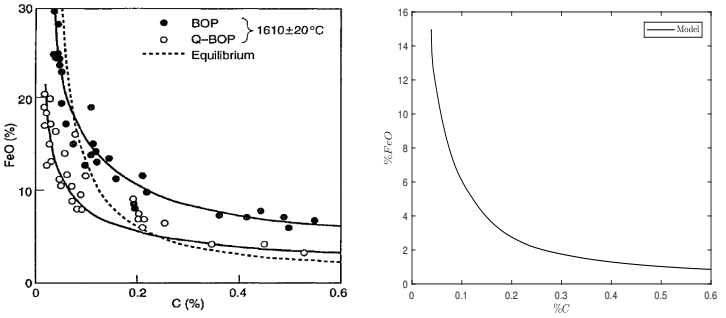

Figure 4.19: Correlation between iron oxide and carbon content in literature (left) and model (right), literature graph adapted from Turkdogan (2010)

In the previous model, the oxygen utilisation was set to full utilisation, using all of the oxygen blown into the furnace. This led naturally to a higher iron oxide content in the slag during the heat, but it also led to that the endpoint content of iron oxide being higher than measured. A possible way of solving this is to have a varying degree of oxygen utilisation during the heat. Decreasing the oxygen utilisation with decreasing carbon content may cause the iron oxide content in the slag to keep a higher level during oxygen blowing and match the measurements.

Fume and Cooling System

The fume's temperature profile matches the measurement to some degree, as presented in Figure 4.12. In order to match the increasing fume and cooling water temperature, a metal layer between the fume and cooling water was added. This acts as a time constant for both of the temperature profiles as this layer takes some time before reaching the fumes temperature. Even though this improved the results, it still lacks some of the characteristics in the measurements. It is hard to pinpoint the reason for this delay in temperature increase for the fume. The waste gas volume flow in the off-gas channel is not measured, nor is the power delivered to the fan. The flow in the model is set to a constant value, but it can be expected that the volume flow in the channel decreases when the fume's temperature increases. The post-combustion is modelled to occur instantly with full combustion, and that the reaction receives all the necessary oxygen from either the process or as false air from the surroundings. This may be a too strong assumption, and modelling the

reaction with chemical equilibrium may improve the results. By doing this, it may slow down the reaction until it receives enough oxygen for full combustion.

The lack of increase in fume temperature is evident in the cooling waters temperature as this remains at a constant level during blowing. For the waste gas hood's cooling water, the temperature does not reach the same level as the measurements. There are some uncertainties in the design of the cooling system, as there is a lack of technical drawings of the system such as cooling pipe radii and the layout of these pipes.

4.10.2 Phosphorus Equilibria

There has been done much work in trying to find an equilibrium for the phosphorus during the production of steel. However, these equilibria vary highly and often only applies for a certain type of slag and other processing conditions. For the phosphorus partition ratios and activity coefficients presented in Table 4.1 and 4.2, only a few gave promising results that were numerical stable during simulation. It is expected that the phosphorus reaction is heavily dependent on the CaO and FeO content, and the dephosphorisation decrease with increasing temperature due to its endothermic nature of the reaction. The reaction rate should, therefore, be low during mid-heat as the slag temperature is high and the FeO content is low, while it is expected to be high at the start and end of the heat. The different equilibria were tested with two different heats that have different additions during the heat. None of the activity coefficients gave promising reaction rates results. By modelling the reaction rate with activities of the species, the rate is very vulnerable to changes in the iron oxide content as this is raised to the power of five. Hence, small changes in the iron oxide content have large effects on the dephosphorisation rate. For the partition ratios reaction rates presented in Figure 4.15, many of them gave promising results.

For the partition ratio number three and five, the corresponding reaction rate kept a relatively high value throughout the heat, not corresponding to the expected kinetics and resulted in too low phosphorus content, compared to measurements. For partition ratio number eight, the reaction rate was nearly linearly increasing from a negative rate until about 80% of the heat. Here, the reaction rate became stiff and numerically unstable. This relates to the relatively high dependency on total iron in the slag phase compared to the other partition ratios, in combination with low CaO dependency and low constant term. Partition rate number four, seven and the adjusted version of number two, number thirteen, all corresponded well with the kinetics given in literature and measurements given by SSAB. The phosphorus content decreases at the start of blowing, before increasing again and remaining constant until towards the end of the heat, where it decreases to below $\approx 0.01\%$. Number four and thirteen gave very similar results and corresponded well with measurements. However, number thirteen was chosen as the partition ratio used for this model since it corresponded better with measurements and is simpler than number four.

4.10.3 Emulsion Height

The emulsion height in the model was modelled according to Equation 4.3.3. The values used for the viscosity and surface tension of the slag were averages from several different slag measurements given in Jung and Fruehan (2000). SSAB does not have any measurements of the emulsion height during heats. Hence the height is compared to what is expected from literature such as Brämming (2010) and what can be expected with regards to the converters geometry. The resulting emulsion height has a reasonable value and does not indicate slopping. The profile also matches what could be expected, as the lance height in the start is higher, resulting in larger iron oxide production and higher decarburisation rate.

4.10.4 Lining Temperature

It is expected that the temperature outermost in the lining remain about constant through and in between heats, while the temperature in the working lining vary with the temperature of the bath. This matches well with the results presented in Figure 4.17. The temperature for $T_{80\%}$ and T_{out} remains nearly constant. The temperature profile of $T_{0\%}$ and $T_{10\%}$ is highly correlated with the bath's temperature profile, which is as expected as this takes up a large amount of the volume and has a larger heat transfer coefficient than the slag and gas phase. Due to the large volume of the $T_{30\%}$, it has a slower temperature profile and does not reach as low temperature as the two innermost temperature profiles.

4.11 Conclusions

Due to the harsh and extreme environment of the BOF process, there is a lack of instrumentation. For the plant studied, the measurements available for heat are the end-point steel composition, possible slag analysis and the off-gas systems temperatures. With the lack of measurements, the BOF process has been operated based on experience and the operator's knowledge about the previous batches accuracy. However, with a model based control system, a state estimator can use the model to predict the process behaviour and update the model with the available measurements. In this chapter, a model has been further developed and compared against process data from a steel plant. The main foci of the modelling were to create a complete model which could replicate the process behaviour and correctly predict the steel composition and temperature. Comparing the model results with the given data, the model produced good results for most of the batches simulated. For some batches, the model deviated from the measurements. Further investigation showed that this might be a result of the loss of bottom stirring in the converter. For the slag composition, the model results correlated well with the batches with slag analysis. However, the iron oxide content in the slag during oxygen blowing was lower than what is expected. The fume temperature profile does not match the measured temperature profile, and without more information about the off-gas duct and its cooling system, it is hard to identify the problem.

Several phosphorus equilibria were investigated with the model. Two partition ratios were found to give the best fit by comparing the results from this with the process data and the suggested profile in literature. Partition ratio number 4 and 13. The model was augmented with continuous monitoring of the temperature in the converters lining. The lining's temperature matched the expectations, with higher variations closer to the metal bath. In addition, a model for the emulsion height was implemented. The emulsion height model produced reasonable emulsion heights that did not correspond to slopping.

Chapter 5

Predictive Monitoring

This chapter describes Cybernetica's tools for simulation, estimation and control, and how the estimator and controller has been designed. The results from the estimation and control cases is presented, followed by a discussion and conclusions.

5.1 Setup

5.1.1 Utilised Software

Cybernetica has several tools to support the development of the model, estimator and controller.

Modelfit

For model validation and offline estimation, Cybernetica's Modelfit is used. Modelfit is used for estimating the parameters assumed to be constant, which parameters should be estimated online and designing the online estimator part of Cenit applications. Modelfit supports multiple data sets from different operating conditions, allowing to find the best parameter fit for all conditions considered.

Cenit

Cenit is a powerful and versatile software suite for nonlinear model predictive control. Since it uses nonlinear mechanistic models, it is a better and more robust alternative to technologies that rely on linear models. The Cenit application consists of a user interface and a kernel. The interface displays the measurements, estimates and control inputs. The kernel communicates with the user interface, and handles the data transfer with the OPC server, database and the process model. The Cenit application is built on top of Cenit SDK. Cenit SDK is a collection of calculation models used in estimation and nonlinear model predictive control. Several interfaces can be implemented, depending on which calculation

modules that shall be used. It is possible to implement different models for each interface, i.e. the controller has a simpler model than the simulator. Cenit SDK consists of interfaces for simulation, Kalman filtering, moving horizon estimation, NMPC, Modelfit and async data.
The model is implemented in the model template in Cenit. In this template all the necessary calculations and the differential equations presented in the previous section is implemented. In addition, it contains different solvers for ODE.

RealSim

Cybernetica RealSim is a plant replacement simulator used for testing of the Cenit modules. RealSim and Cenit communicates through OPC in order to replicate a distributed control system. As mentioned, the simulator may use a different model than the model implemented in the controller. In this project the simulator and controller use the same model. The noise added to the system is implemented in RealSim's simulator interface.

5.1.2 Implementation

Through Cybernetica's tools, the model has been validated and adjusted, and the estimator and controller have been configured. Using Modelfit, the parameters in the model have been adjusted using an optimisation tool in addition to trial and error. After this, the results from model fitting has been validated against the measurements given by SSAB. These datasets are the same as used during the preliminary report. During simulation, RealSim and Cenit are used. RealSim simulates the data and sends the data to the local OPC server where Cenit can read the measurements, inputs and outputs. After the estimator and controller is finished with the calculation, Cenit sends the new control inputs to the OPC server, and RealSim can apply this to the model. During the simulation, Cenit logs the selected data to a local SQL database. This is illustrated in Figure 5.1.

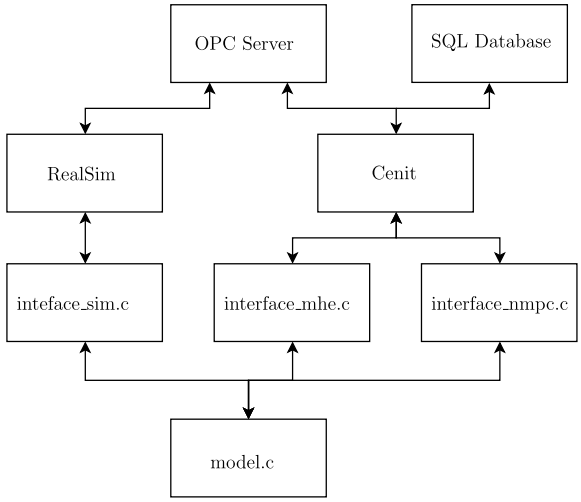

Figure 5.1: Communication between interfaces, model and software

The model presented in the previous section is implemented on the following form in Cenit SDK. The solver used for integration for this model is the 2nd order Runge-Kutta.

$$\begin{aligned} x_k &= f(x_{k-1}, u_{k-1}, \theta, v_{k-1}) \\ y_k &= g(x_k, u_{k-1}, \theta) + w_k \\ z_k &= h(x_k, \theta, u_{k-1}) \end{aligned} \tag{5.1.1}$$

where

$$\begin{aligned} x_k &= \text{Model states at time } t_k \\ \theta &= \text{Model parameters} \\ u_{k-1} &= \text{Process inputs from } [t_{k-1},\, t_k] \\ y_k &= \text{Measurement at time } t_k \\ v_{k-1} &= \text{White process noise} \\ w_k &= \text{White measurement noise} \\ z_k &= \text{Output variable (CV)} \end{aligned} \tag{5.1.2}$$

5.1.3 Heat Recipe

In order to have full faith in the measurements and no uncertainties in weights or gas injected, a heat recipe was created to simulate data. This also enables to use the waste gas measurements to indicate the possibilities with these measurements. The recipe was created by the author, and is inspired by the pattern given in literature, such as (Turkdogan, 2010), and the data given by SSAB. In order to keep the data from SSAB confidential, the heat recipe has been altered.

The inputs to the system (MV) is presented in Table 5.1.

Table 5.1: Model inputs

Index	MV	Description	Unit
1	Q_{O_2}	Oxygen blown by lance	$[Nm^3/min]$
2	L_h	Lance height	$[m]$
3-8	Q_i	Injection gases in bottom	$[Nm^3/s]$
9-15	w_i	Addition rate	$[kg/s]$
16	T_c	Cooling water inlet temperature	$[K]$
17	t_{O_2}	Oxygen blowing time	$[s]$

The injection gases are bottom injection of different gases, only Ar and N_2 are used. Addition of different fluxes such as pellets, lime and dolomite and scrap are available. Cooling water is the water inlet temperature in to the cooling system in the off-gas system. t_{O_2} is the blowing time for the batch.

The oxygen flow rate and lance height recipe is presented in Figure 5.2.

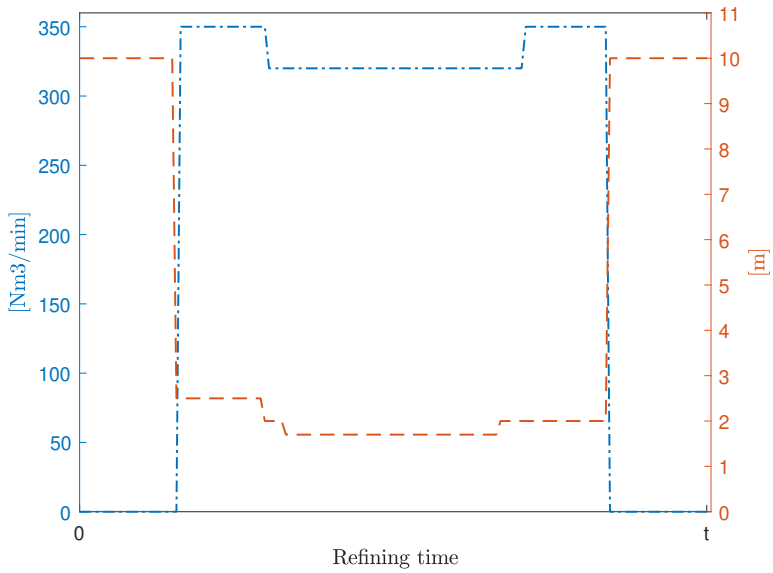

Figure 5.2: Oxygen and lance height profile

The injection of argon and nitrogen is presented in Figure 5.3.

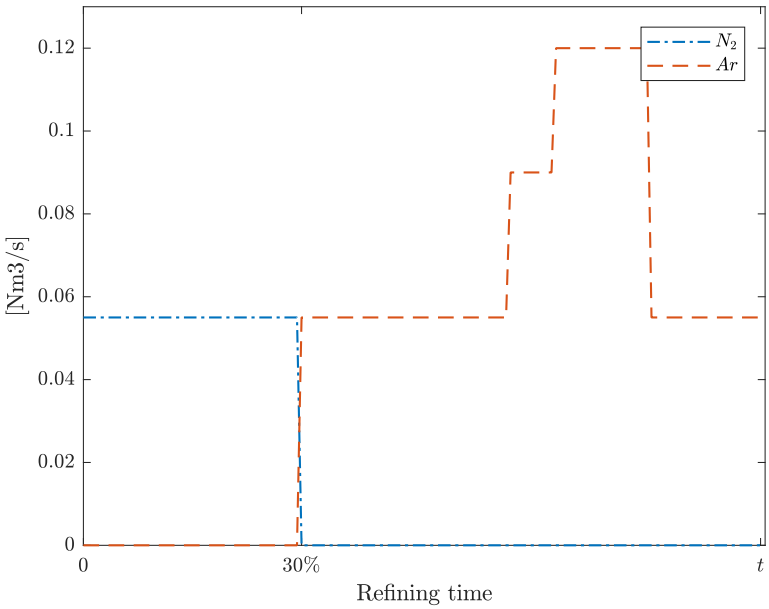

Figure 5.3: Injection of Argon and Nitrogen

The amount of hot metal added to the converter with its content and the amount of additive materials is presented in Table 5.2.

Table 5.2: Batch details

Initialization	
Hot metal	104000 kg
Slag	0
%C	4.5
%Si	0.6
%Mn	0.18
%P	0.061
%S	0.009
Scrap	26000 kg
Temperature	1350℃
Total additions	
Lime	6500 kg
Pellets	3000 kg

5.2 MHE

In this section, the configuration of the moving horizon estimator is presented. The state-space model is presented in Equation 5.1.1. The measurement and output model is the same. For the estimator, the system and its parameters are subject to additive white noise,

$$\begin{aligned} x_{k+1} &= f(x_k, u_k, \theta_k) + v_{s,k} \\ \theta_{k+1} &= \theta_k + v_{p,k} \end{aligned} \tag{5.2.1}$$

The state vector is augmented with the parameters to facilitate for parameter estimation. $v_{s,k}$ and $v_{p,k}$ is the noise added to the states and parameters. The system is subject to the constraints

$$\begin{aligned} \hat{x}_{low} \leq \hat{x} \leq \hat{x}_{high} \\ \theta_{low} \leq \theta \leq \theta_{high} \\ u_{low} \leq u \leq u_{high} \\ y_{low} \leq y \leq y_{high} \\ v_{min} \leq v \leq v_{max} \end{aligned} \tag{5.2.2}$$

The optimisation problem for the MHE then becomes,

$$\Phi_T = \min_{x_0,\ldots,x_T} \Gamma(x_0) + \sum_{k=0}^{T-1} v_k^\top V_k^{-1} v_k + \sum_{k=0}^{T} w_k^\top W_k^{-1} w_k \tag{5.2.3}$$

where

$$\Gamma(x_0) = (x_0 - \hat{x}_0)^\top \Pi_0^{-1} (x_0 - \hat{x}_0) \tag{5.2.4}$$

Π_0 is the state covariance matrix, initialised by σ_{x_0} and σ_{θ_0},

$$\Pi_0 = \mathbb{E}\{[x_0, \theta_0]^\top [x_0, \theta_0]\} = diag([\sigma_{x_0}, \sigma_{\theta_0}]) diag([\sigma_{x_0}, \sigma_{\theta_0}]) \tag{5.2.5}$$

Where σ_{x_0} and σ_{θ_0} are tuning parameters for the estimator. For $T > N$, 0 denotes $T - N$.
The process and measurement noise covariance matrices are defined as,

$$V_k = \mathbb{E}\{v^\top v\} = diag(\sigma_v) diag(\sigma_v) \tag{5.2.6}$$

$$W_k = \mathbb{E}\{w^\top w\} = diag(\sigma_w) diag(\sigma_w) \tag{5.2.7}$$

In this project, no specific states are estimated. Instead, the parameter estimates handle the possible deviation in measurements and estimates. By doing this, the energy and mass balance are still valid. The parameters to be estimated in this project are the oxygen utilisation (η) and/or the bottom stirring efficiency (η_b). These parameters are expected to be varying between batches. The oxygen utilisation is assumed to be varying with a Gaussian distribution, while the bottom stirring efficiency is assumed to have a degrading efficiency before maintenance, where the efficiency then increases again. This assumption is based on the data

given by SSAB on the carbon-oxygen factor (4.2.1) for a series of batches, where there is a similar trend. The entries in the covariance matrix with their corresponding constraints is then,

Table 5.3: Non-zero MHE tuning parameters

Variable	**Type**	$\boldsymbol{\sigma}$	[low, high]
η	Parameter	0.01	[0.8, 1]
η_b	Parameter	0.05	[0.1, 1]

The process noise is assumed to be additive in the estimator. The noise added to the states are listed in Table 5.4. The number of blocks are the number of parameters used to parameterize the process noise in the horizon.

Table 5.4: MHE process noise tuning parameters

Disturbance	$\boldsymbol{\sigma}$	**Blocks**
v_η	1.3e-5	No. of batches
v_{η_b}	1.8e-5	2

Here v_η is the process noise on the oxygen utilisation parameter and v_{η_b} is the process noise on the bottom stirring efficiency.

For the process the actual measurements are listed in Table 5.5. These measurements are measured after the batch is finished, hence the only measurement update for the MHE is after finished blowing and the system has stabilized. This makes the estimation problem harder as the estimator has no measurement updates during blowing. For the process considered the only measurements during blowing are the waste gas and cooling system measurement. Since there are some uncertainties with these measurements and the model's results are not corresponding well with the process, these measurements are not used. The uncertainty related to the measurements, σ, is roughly set to 1% of the final value.

Table 5.5: Mean and variance of measurements

Measurement	σ	Unit
Steel		
Steel mass	1000	kg
C	0.0001	%
Si	0.00001	%
Mn	0.001	%
P	0.0001	%
S	0.00001	%
Steel temp	10	°C
Slag		
FeO	0.1	%
SiO_2	0.1	%
MnO	0.01	%
P_2O_5	0.01	%
CaO	0.1	%
MgO	0.01	%
Fe_2O_3	0.01	%
Fume		
Fume temp	30	°C

5.3 NMPC

The general NMPC optimisation problem with the model given in Equation 5.1.1 takes the form,

$$\min_{\Delta U} J(Z, \Delta U) = \min_{\Delta U} 0.5(Z - Z_{ref})^\top Q(Z - Z_{ref}) + 0.5\Delta U^\top S \Delta U + r_1^\top \varepsilon + 0.5\varepsilon^\top diag(r_2)\varepsilon \quad (5.3.1)$$

where

$$Z = [z_T, z_{T+1}, \ldots, z_{T+N}] \quad (5.3.2a)$$

$$\Delta U = [\Delta u_T, \Delta u_{T+1}, \ldots, \Delta u_{T+N}] \quad (5.3.2b)$$

Z is the predicted output in the prediction horizon and Z_{ref} is the reference trajectory. ΔU is the optimal input trajectory for the control horizon and ε is the maximal constraint violation of each z variable. The matrices Q and S are the normalized output and input weights and r_1 and r_2 are the linear and quadratic constraint violation weights.

Objective Function

The main control objectives are to achieve steel temperature and carbon content within the specification even with changing process factors such as oxygen utilisa-

tion and bottom stirring efficiency. For this, the CV to be controlled is the carbon content for the entire metal bath, and with a given recipe, this can be achieved by optimising the oxygen blowing time. Therefore the objective function can be written as,

$$J(Z, \Delta U) = \sum_{0}^{N_P} 0.5(\%C - \%C_{sp})^2 q + \sum_{0}^{N_C} 0.5\Delta t_{O_2}^2 s + r_1^\top \varepsilon + 0.5\varepsilon^\top diag(r_2)\varepsilon \tag{5.3.3}$$

where N_P and N_C is the prediction- and control horizon. $\%C_{sp}$ is the carbon content set-point and t_{O_2} is the oxygen blowing time. In addition to defining the optimisation problem, we need to define how often the optimisation problem should be solved. The sampling time of the controller should be fast enough to incorporate the system's behaviour. Therefore, the sampling time should be much shorter than the time constant of the CV we want to control. One should also keep in mind the computation time necessary to finish the optimisation problem. The computational load is dependent on the free optimisation variables, the prediction- and control horizon and the parameters used to parametrise the horizon. The dynamics of the carbon content in the metal is quite slow. Therefore the sampling interval for the MPC can be extended. For this project, the sampling interval is $10s$.

Since the control objective is focusing on the endpoint value and not the trajectory, it is practical to choose the prediction horizon long enough to predict the endpoint carbon content and only weight the last sample.
For the control horizon, it is also favourable to have a long horizon so that the process is controlled with respect to the endpoint specification. The controller is only optimising the blowing time, which should ideally keep a constant value throughout the batch, hence it is weighted on the current sample. For the other control inputs, they are read from the recipe, therefore these values are only weighted on the last sample of the horizon. This is summarized in Table 5.6.

Table 5.6: Control and prediction horizon

Horizon	**Weighted samples**	**Length**
Control	149	24 min 50 s
Control(t_{O_2})	0	24 min 50 s
Prediction	150	25 min

Configuration of MV and CV

The weights, nominal value and target of the MV and CV are listed in Table 5.7. With two variables in the objective function, it is fairly straightforward to set the weights. Since the target is to achieve the desired carbon content in the steel, the deviations from the set-point is set much higher than the cost of changing blowing oxygen. This, in addition to the nominal value of the MV, ensures that the controller quickly finds the optimum.

Table 5.7: Configuration of MV and CV

Parameter	t_{O_2}	$z[\%C]$
weight	1e-6	1e3
nominal value	$\max(t_{O_2}, 10 \text{ min})$	-
target	-	0.035%

The constraints on the input and output are listed in Table 5.8.

Table 5.8: Constraints on MV and CV

Constraint	t_{O_2}	$z[\%C]$
min	1 min	0
max	30 min	100

5.4 Simulations

The tests are simulated with a fixed recipe set by the author for each heat, as presented in Section 5.1.2. The main goal for the estimator is to predict the correct oxygen utilisation η, and the correct bottom stirring efficiency η_b, and hence predict the correct amount of carbon content in the metal. For the controller, the aim is to calculate the optimal blowing time for the heat with the estimated parameters to achieve the desired carbon content. The estimator results are simulated using Modelfit, while the optimal control cases are simulated using RealSim and Cenit, as described in Section 5.1.2.

The variation of oxygen utilisation and bottom stirring efficiency is presented in Figure 5.4. The degrading efficiency in the bottom stirring should replicate the process' behaviour when the bottom tuyeres start getting clogged before having maintenance, and the efficiency improves.

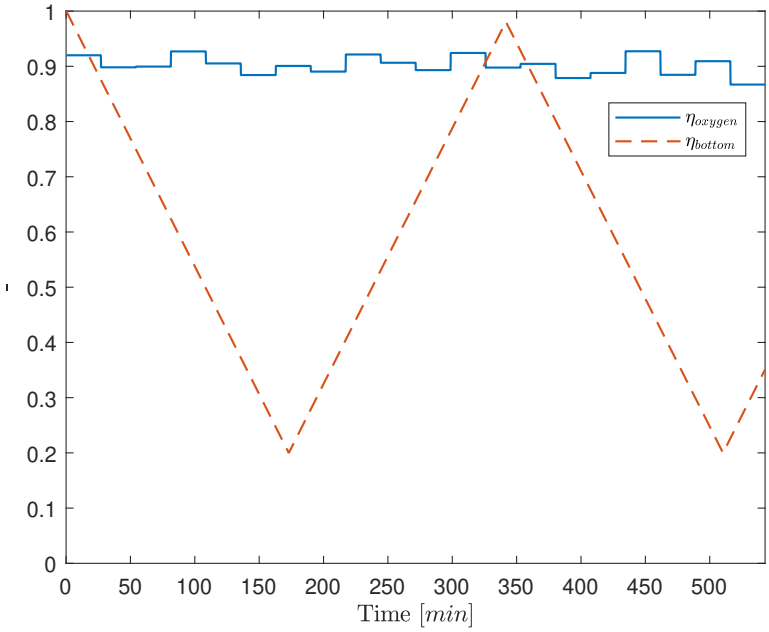

Figure 5.4: Variation of oxygen utilisation and bottom stirring efficiency

In order to demonstrate the capabilities and limitations with the estimator and limited amount of measurements, the estimator is tested with different disturbances and measurements. These cases are listed in Table 5.9. The optimal control cases are based on the estimator cases and are listed in Table 5.10.

Table 5.9: Estimation and control cases with configuration of MHE

Case	Disturbance	Estimator setup						
		σ_η	v_η	Blocks	σ_{η_b}	v_{η_b}	Blocks	Horizon
1	Intial offset in η	0.01	0	1	0	0	0	3 batches
2	White noise on η	0.01	1.3e-5	3	0	0	0	3 batches
3	Decreasing and increasing η_b	0	0	0	0.2	0	1	3 batches
4	Varying η and η_b	0.01	0	1	0.05	0	1	1 batch
5	Varying η and η_b	0.01	1.3e-5	3	0.05	1.8e-4	2	3 batches
6	Varying η and η_b with slag meas.	0.01	1.3e-5	3	0.05	1.8e-4	2	3 batches
7	Varying η and η_b with fume meas.	0.01	1.3e-5	3	0.05	1.8e-4	2	3 batches
8	Varying η and η_b with sub-lance meas.	0.01	1.2e-5	3	0.05	1.5e-4	2	3 batches
9	50% reduction in carbon reaction constant	0.01	0	1	0	0	0	3 batches
10	Initial error in metal content with fume meas.	0.05	1.0e-5	3	0	0	0	3 batches

Table 5.10: Optimal control cases

Case	Disturbance	Measurement	Estimator setup	Controller setup
11	Decreasing and increasing η_b	End point steel	Case 3	$z_{sp}[\%C]$
12	Varying η and η_b	End point steel and slag	Case 6	$z_{sp}[\%C]$
13	Varying η and η_b	End point steel and slag with cont. fume	Case 7	$z_{sp}[\%C]$
14	Varying η_b and sine varying η	End point steel and slag	Case 6	$z_{sp}[\%C]$
15	50% reduction in carbon reaction constant	End point steel and slag	Case 9	$z_{sp}[\%C]$
16	Initial error in metal content and varying η_b	End point steel and slag with cont. fume	Case 7	$z_{sp}[\%C]$
17	Initial error in metal content	End point steel and slag with cont. fume	Case 10	$z_{sp}[\%C]$

5.5 Results

In this section, the results from the estimation and optimal control cases in Table 5.9 and 5.10 are presented.

5.5.1 Estimation Results

Estimation of η

The initial configuration of the estimator was done in Modelfit with the cases listed in Table 5.9. The estimator performance for an initial offset in oxygen utilisation is presented in Figure 5.5.

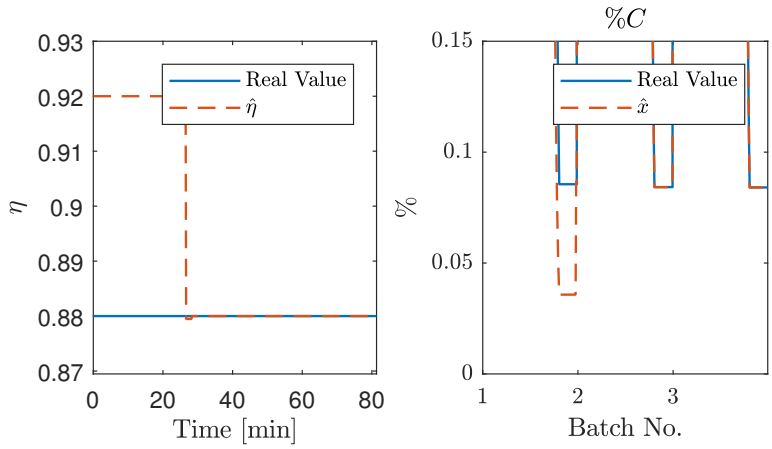

Figure 5.5: Estimation with an initial offset in η, case 1

Figure 5.6 presents the estimation results of applying white noise on the oxygen utilisation parameter, η. Furthermore, it presents the estimated carbon content of the metal against the real value.

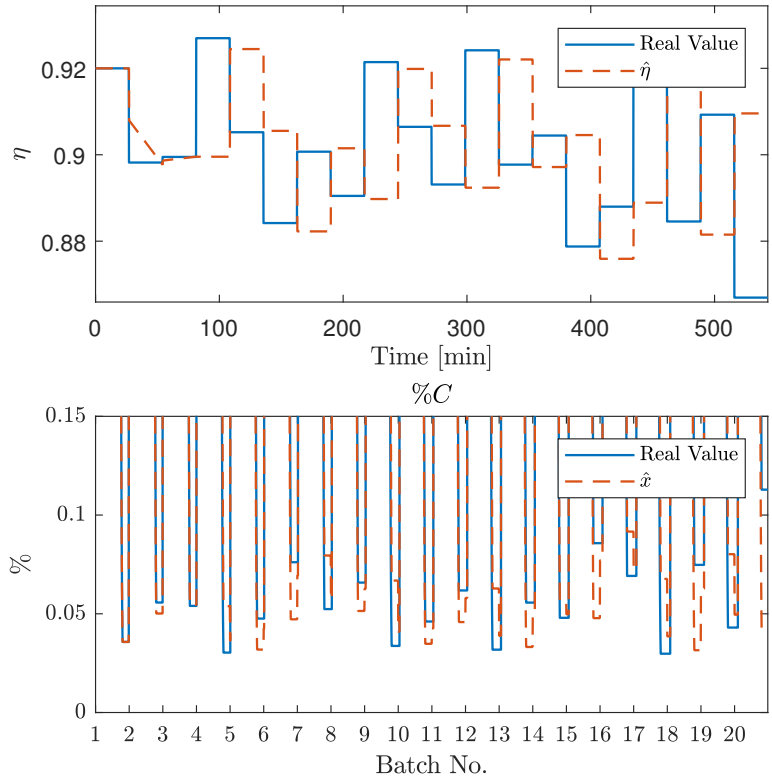

Figure 5.6: Estimation with varying η, case 2

Estimating η and η_b

Figure 5.7 and 5.8 presents the online estimation of the oxygen utilisation η and the bottom stirring efficiency, η_b, for the estimation cases 4, 5 and 6. In addition, it presents the estimated carbon content of the metal and the estimation error of carbon.

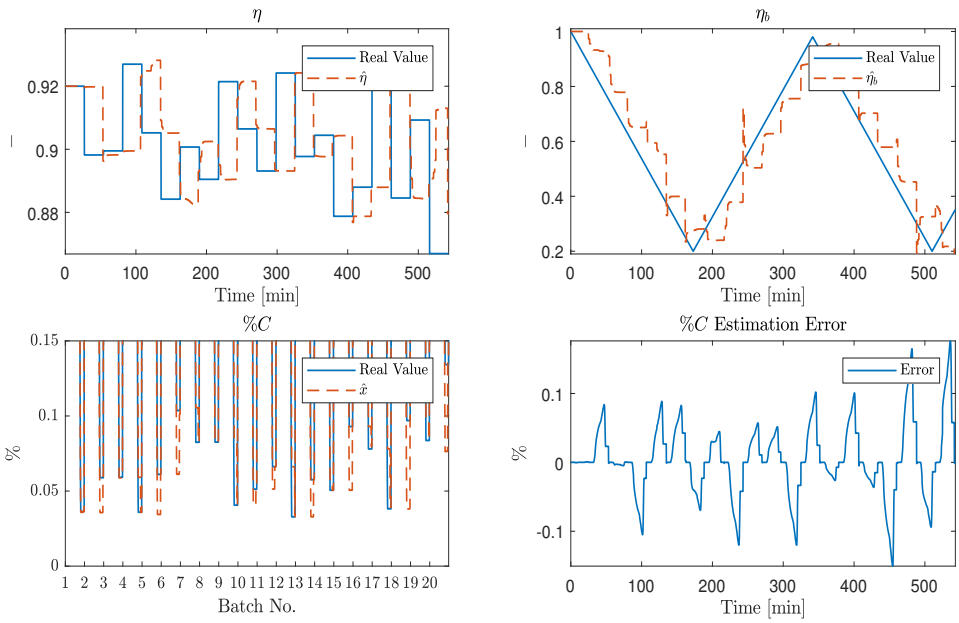

Figure 5.7: Estimation with varying η and η_b, case 4

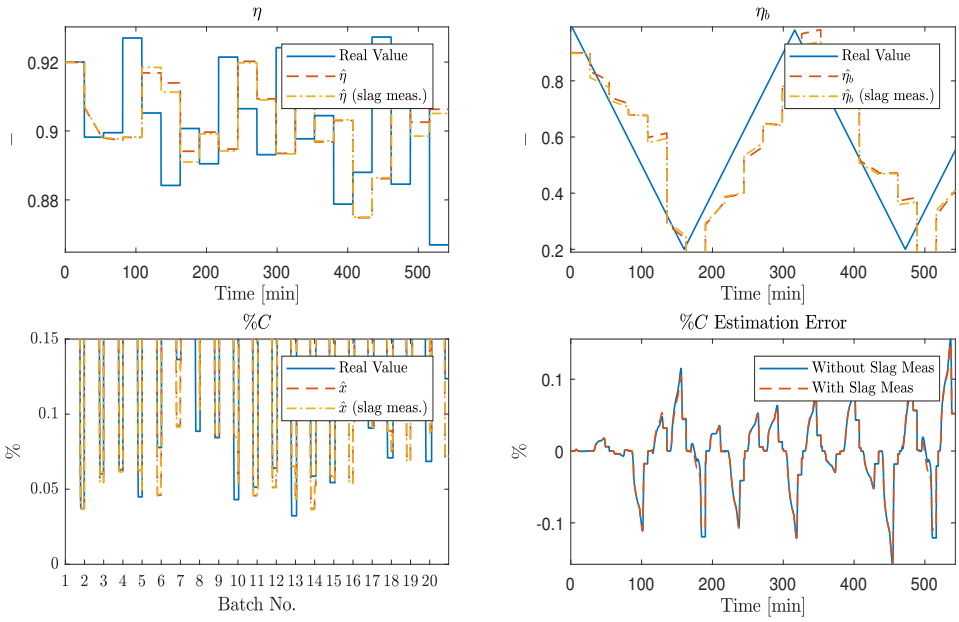

Figure 5.8: Estimation with varying η and η_b, case 5 and 6

Lance Measurement

Figure 5.9 presents the results from adding a sub-lance measurement of the steel four minutes before the planned end of the heat. The same disturbances are applied to the bottom stirring and oxygen utilisation as the earlier results without sub-lance measurement.

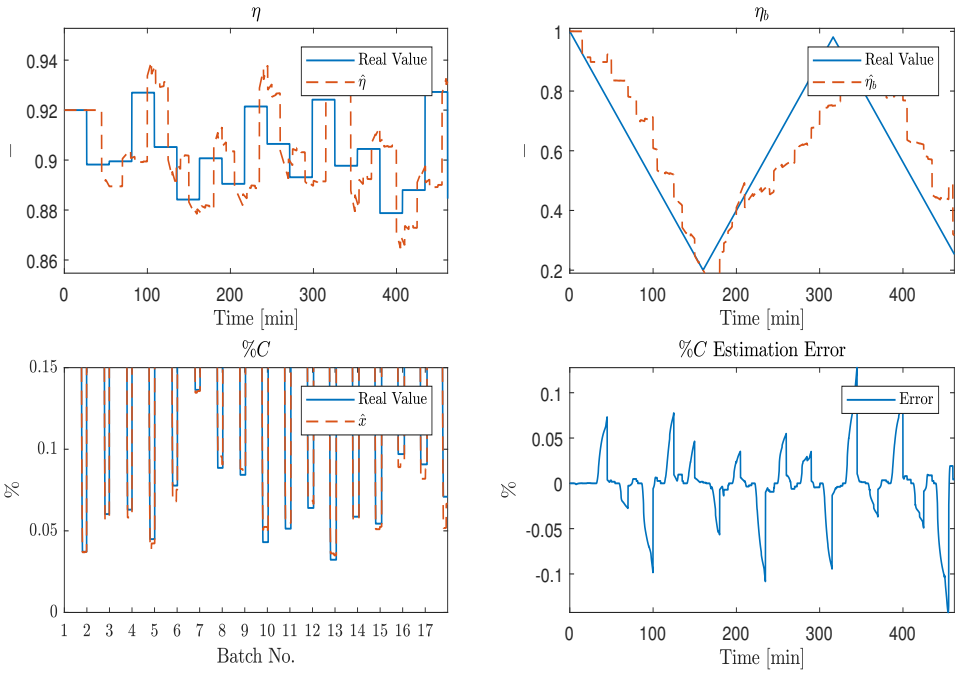

Figure 5.9: Estimation results for varying η_b and η with lance measurements, case 8

5.5.2 Control Results

Perfect model without disturbances

The control results using a perfect model without any disturbances is presented in Figure 5.10. The temperature profile of the metal bath is presented along with the fume temperature, carbon content and iron oxide content.

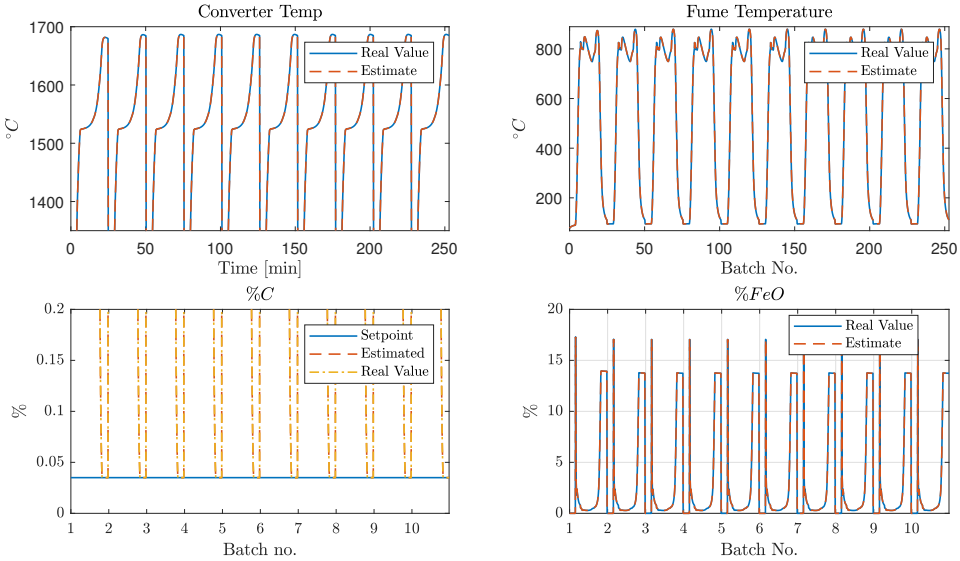

Figure 5.10: Estimation and control results with perfect model

Reduction in decarburisation constant

Figure 5.11 presents the results from having an initial error in the offline estimate of the decarburisation constant.

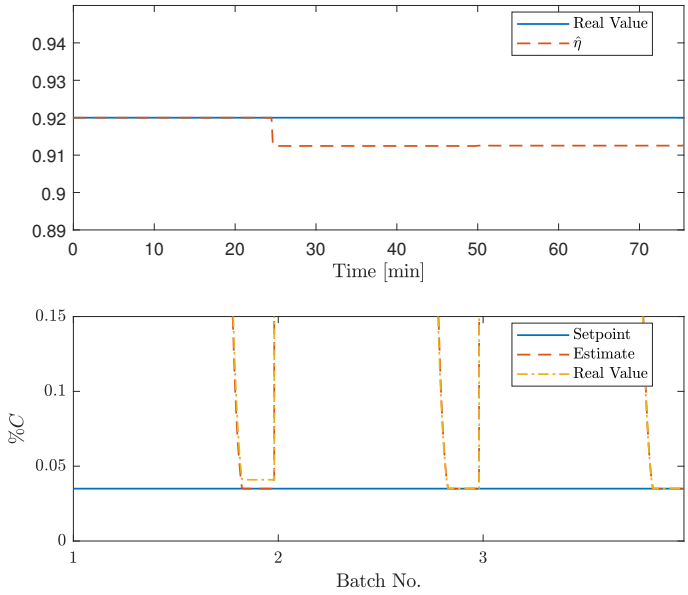

Figure 5.11: Estimation and control results for 50% reduction of decarburisation constant, case 15

Varying η_b

Figure 5.12 presents the results from estimating the bottom stirring efficiency with only end-point measurements. It presents the online estimation of the bottom stirring efficiency and how the controller deviates from the set-point. The real values presented in the graphs are the values used by the simulator.

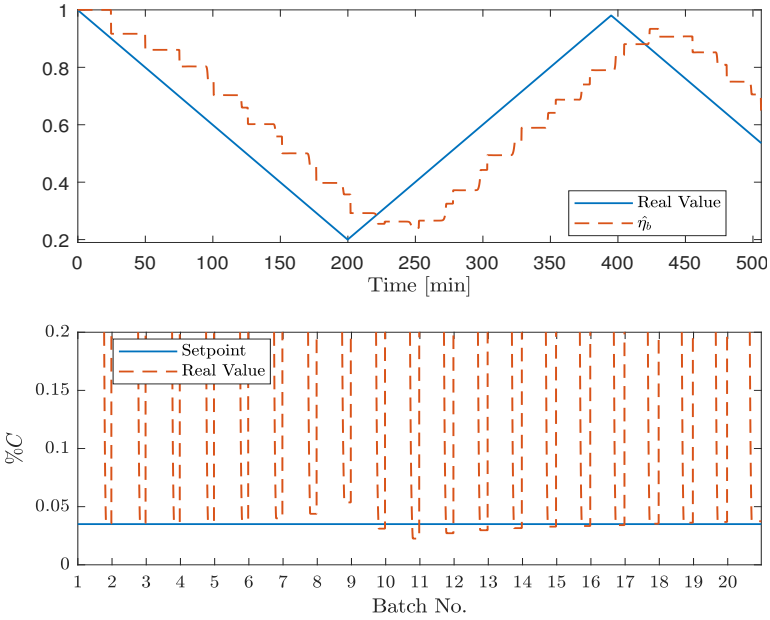

Figure 5.12: Estimation and control results with varying η_b, case 11

Varying η and η_b

The control results for endpoint with slag measurement and without estimation is presented in Figure 5.13. The error plot presents the simulated carbon content deviation from the set-point, with and without estimation.

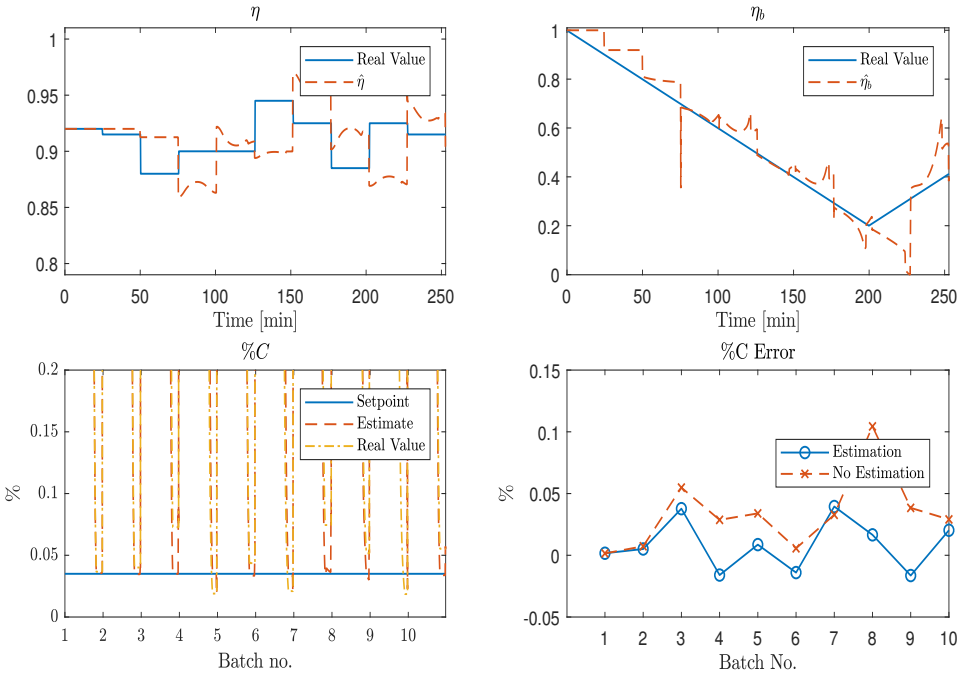

Figure 5.13: Estimation and control results for varying η and η_b with slag measurements, 12

The results from adding the fume measurements is presented in Figure 5.14

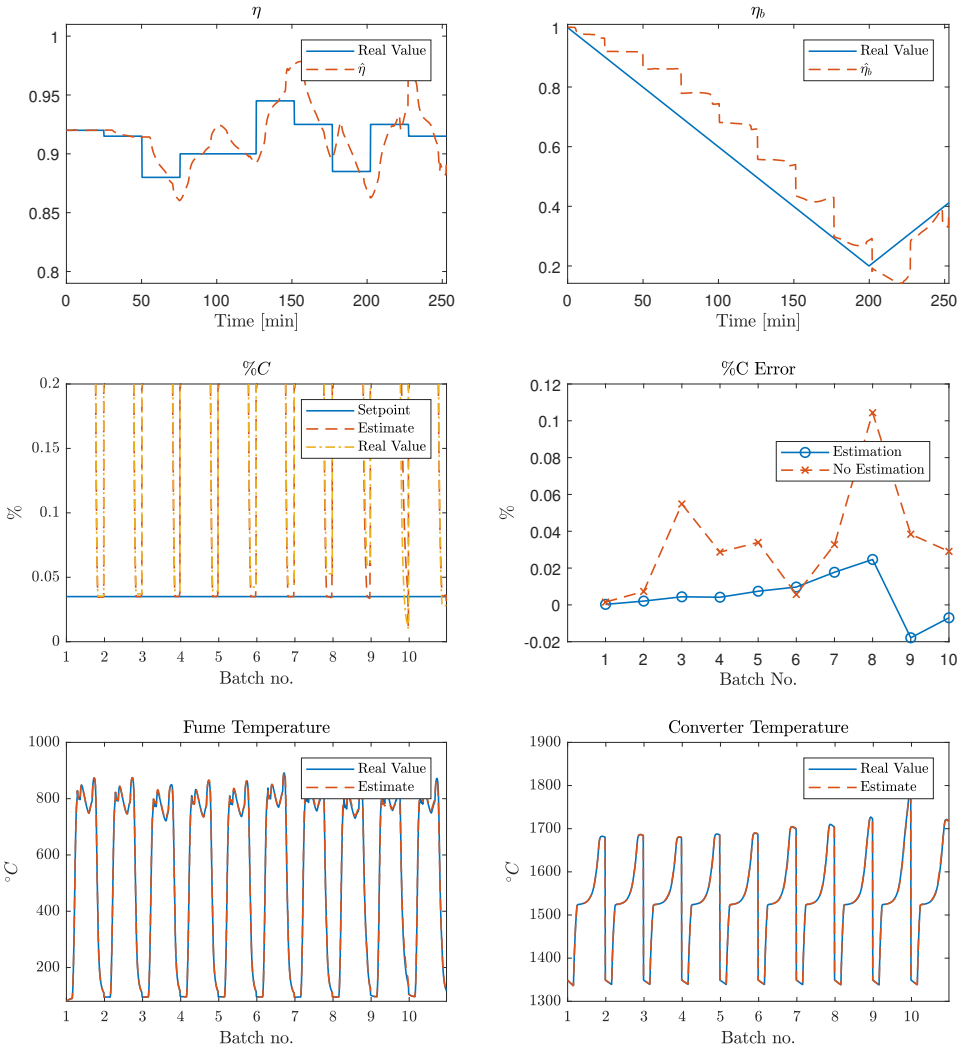

Figure 5.14: Control results for varying η and η_b with fume measurements, case 13

Varying η_b and sine varying η

The results from applying a sinusoidal disturbance to the oxygen utilisation and a varying bottom stirring efficiency are presented against no estimation in Figure 5.15.

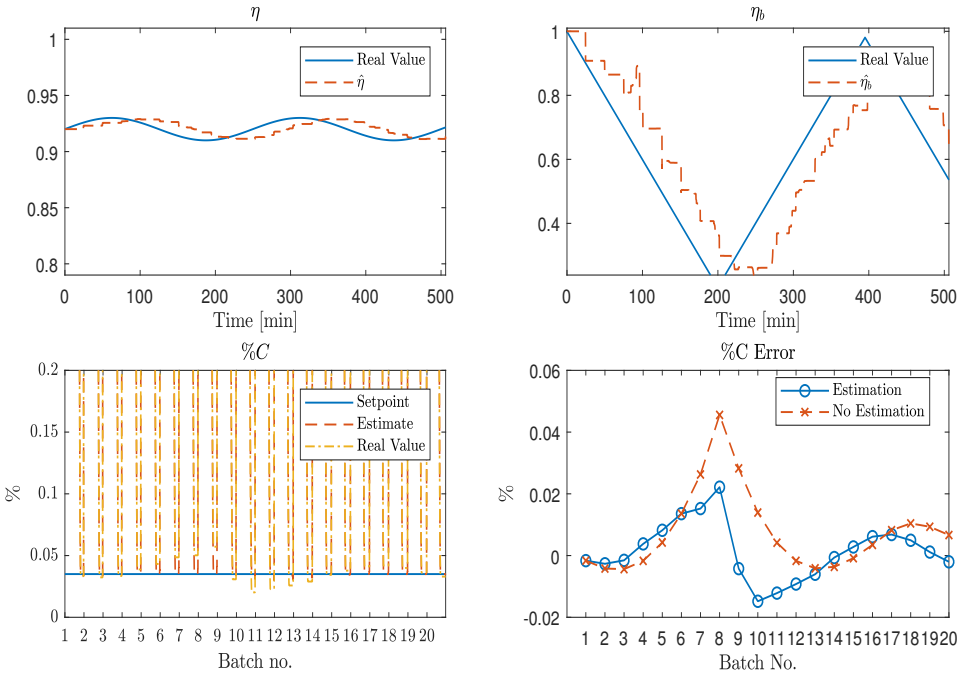

Figure 5.15: Control results with and without estimation for varying η_b and sine varying η, case 14

Initialization Error

It is expected that there are some uncertainties in the initial specification of the metal. The results from applying white noise to the initialisation of the batch are presented in Figure 5.16 and 5.17. These are simulated with continuous fume temperature measurement. Case 16 has also a disturbance on the bottom stirring efficiency. Towards the end of the simulation, the initial error is so significant that both oxygen utilisation and bottom stirring reaches its upper limit.

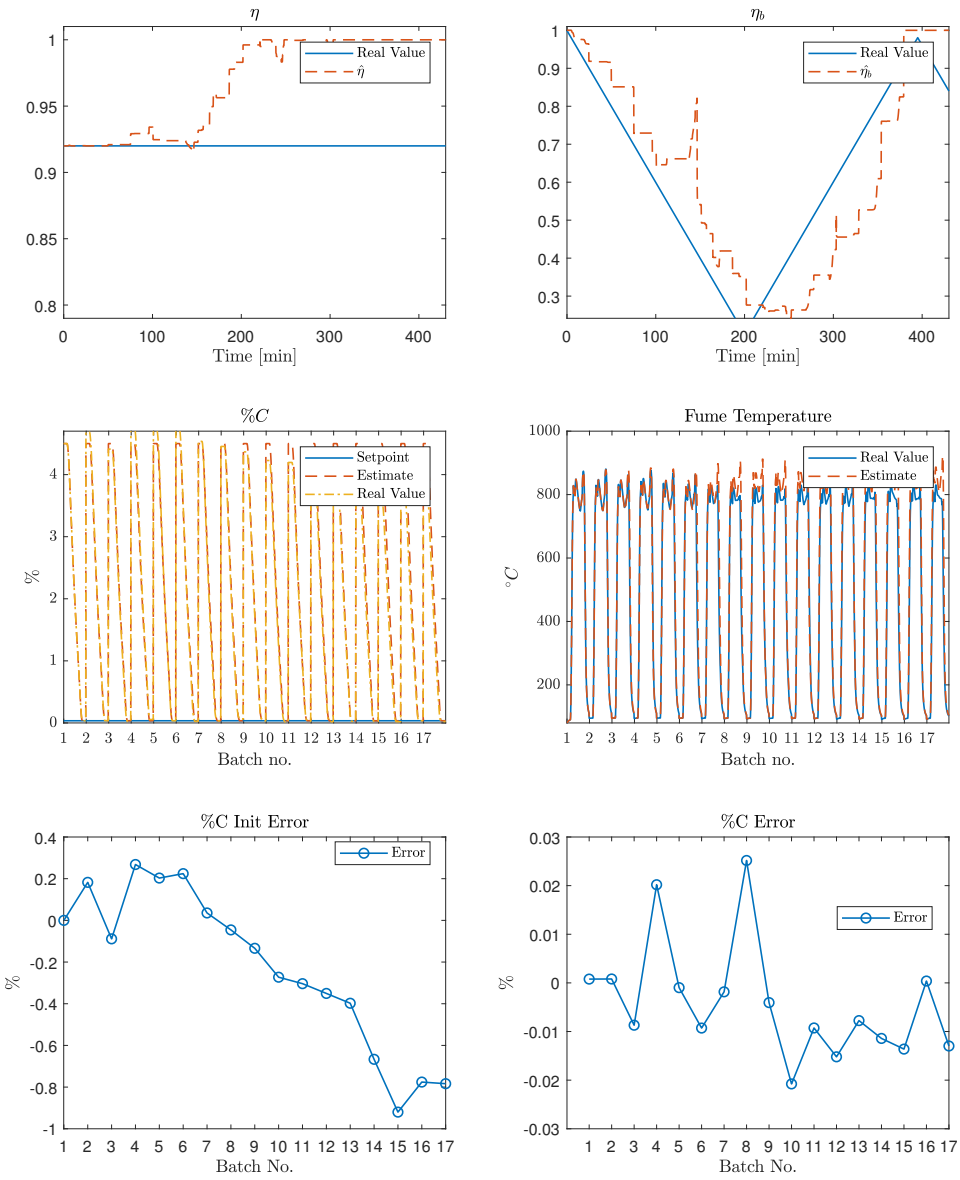

Figure 5.16: Control results for varying η_b and initialization error, case 16

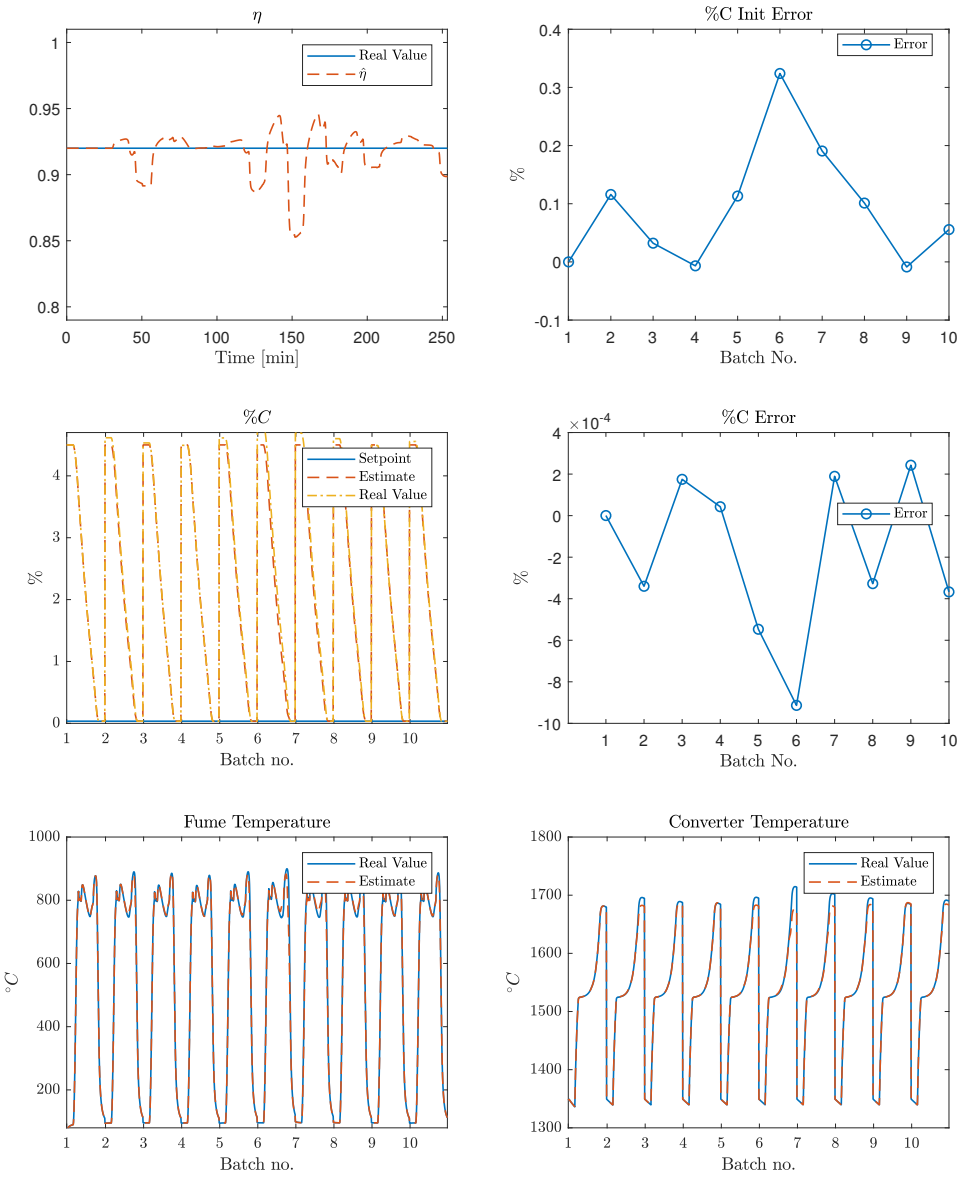

Figure 5.17: Control results for initialization error, case 17

5.6 Discussion

5.6.1 Estimator Results

The availability of measurements is a crucial factor in the performance of the estimator. This is evident in the cases tested with different measurements available. For the cases with end-point steel measurements, the estimator does not update the parameter estimates during the heat, and hence the end result is only affected by the measurements given earlier in the horizon. To verify the configuration of the estimator, a simple case with an offset in the oxygen utilisation parameter is presented in Figure 5.5. The estimator quickly finds the correct parameter value when the measurements become available. If these parameters are affected by independent noise, the estimator is not capable of predicting the next parameter value without any measurements during the heat, resulting in too low or high carbon content. This is presented in Figure 5.6. The cases with disturbances on both oxygen utilisation and bottom stirring is presented in Figure 5.7 and 5.8. In case 4, the estimator had an estimation horizon of one batch. This resulted in that the oxygen utilisation was only updated with the previous oxygen utilisation, leading to large errors in the carbon predictions. In case 5, the estimator had an estimation horizon of three batches. The estimator has issues with estimating both η and η_b for large variations in η, this resulted in large variations in the estimates of the bottom stirring. For the bottom stirring efficiency, it is expected that this parameter is slowly decreasing before maintenance. This slow decrease facilitates a better parameter estimate as presented in Figure 5.12. The results from having a disturbance trend in the horizon is also presented in Figure 5.15. Here the oxygen utilisation, η, has a varying value following a sinusoidal curve with the bottom stirring varying as previously. This results in a considerable better estimate than for independent disturbances, with the estimator being able to predict a reasonable value for both η and η_b.

Figure 5.8 presents the different estimation results for different measurements. If only measuring the end-point steel content, the estimator has an observability problem when estimating both η and η_b. Decreasing the bottom stirring efficiency leads to lower carbon content in the metal, but it also leads to a higher content of iron oxide in the slag due to the low carbon concentration in centre and bulk. By adding a measurement of the slag at the end of the heat, in addition to the steel, the estimator should be able to estimate a better value for these two parameters, and in particular, the bottom stirring. The slag measurements improve the estimate of the parameters, but the estimator still has issues with the large changes in the oxygen utilisation, leading to a rather poor estimate of the carbon content. The fume modelling results did not lead to a good representation of the process' behaviour, but the results using the fume measurements are included to present the possible improvements, the results are presented in Figure 5.14. By using the fume measurements, the parameter estimate has improved. The estimator produces reasonable parameter estimates, and the estimated fume temperature matches the measured. With reasonable parameter estimates, the estimated car-

bon content correlates well with the measured end-point content. This holds true except for when the bottom stirring efficiency changes from decreasing to increasing efficiency, leading to considerable deviations.

There is a significant improvement by adding a sub-lance measurement four minutes before the planned end of the heat, as presented in Figure 5.9. By adding this, the estimator handles the significant changes in oxygen utilisation and the bottom stirring efficiency. For batch number 17, if the changes in oxygen utilisation are too significant, the sub-lance measurement comes too late, resulting in a considerable deviation from the real value.

5.6.2 Control Results

The controller was configured to calculate the optimal blowing time of oxygen with respect to the carbon content in the metal. As there was no economic perspective or any strict constraints on this optimisation problem, the carbon content weights were set high enough to quickly find the optimal time without considering the cost. For a perfect internal model with no external disturbances, the controller satisfied the end-point carbon content specification perfectly, as presented in Figure 5.10.

Without Estimator Feedback

Since there doesn't exist any direct measurement from the converters environment, disabling the estimator is the same as removing the feedback to the controller. Hence, the controller finds the optimal blowing time based on an erroneous model. As presented in Figure 5.14, this results in poor controller performance.

With Estimator Feedback

The ability to estimate an oxygen utilisation to compensate for errors in other parameters was investigated in case 15. As visible in Figure 5.11, the estimator quickly finds the oxygen utilisation to compensate for the offset and the controller achieves the desired end-point content. The control results from using bottom stirring efficiency estimation are presented in Figure 5.12. The parameter estimation is, as discussed earlier, quite good. The controller achieves the desired carbon content in the steel except for when the bottom stirring efficiency changes from having a decreasing efficiency to increasing. This is as expected, as the estimator does not receive any information about maintenance.

For the cases with significant variations in the oxygen utilisation, the estimator does not produce an accurate estimate of the parameters, as presented in Figure 5.13. With only end-point measurements the estimator does not have enough information to produce reasonable estimates of the oxygen utilisation for the batch. This is evident in the carbon error plot, in some cases the results from not having

state estimation is equally good, or even better, as with state estimation. A problem that may arise when estimating significant changes in the oxygen utilisation is the stiffness of the slag reactions. During heat, the iron oxide content in the slag is lower than expected. Increasing the oxygen utilisation has, therefore, a significant effect on the slag reactions, as the iron oxide content in the slag increases. It is also worth noting that for the cases where the resulting carbon content is approximately 0.02%, the equilibrium is reached, and the carbon content does not decrease any more, Figure 4.2. As discussed in the previous section, the results of adding more measurements are much better. The estimator produces a reasonable parameter estimate, resulting in a more accurate carbon content at turn-down, as presented in Figure 5.14.

For the initialisation errors, the simulation was subject to initial error in the total steel weight and the content of the trace species. In addition, the case presented in Figure 5.16 has varying bottom stirring efficiency. The estimation and control results were investigated with respect to the carbon content. The estimator problem was to estimate the oxygen utilisation and bottom stirring efficiency to compensate for the initialisation error and the varying bottom stirring efficiency. The results showed varying precision regarding correcting for the initialisation error, with the resulting end-point carbon content error shifting from negative 0.02% to almost 0.03%. The last simulated batches had a very low true carbon content, resulting in full oxygen utilisation and bottom stirring efficiency. This full utilisation should alarm the operator, as it is very unlikely to have this high utilisation. It is also not expected that the error of the initialisation is in the magnitude of 1% carbon. For initialisation errors of less magnitude and without bottom stirring disturbance, the estimator was able to track the fume temperature perfectly, as presented in Figure 5.17. However, it should be noted that by only estimating the parameter value for oxygen utilisation, the converter's temperature will not match the real value. Although the estimator matches the fume temperature and achieves the desired end-point content, it does not compensate for the difference in carbon content in the metal, which has a significant effect on the converter's temperature.

Computational Load

For the cases with large variations on the oxygen utilisation and the bottom stirring efficiency, a more complex noise model was needed to achieve reasonable estimates and to increase the robustness of the estimator. With the process model developed in this work, this came at a high cost concerning computational load. For case 12 with a sampling time of 10 seconds, the estimator and controller used on average 30 seconds per sample. If this should be applied to a real plant, the design of the control system and the model need to be considered. Creating a simpler model that can have a higher integration step and still replicates the process behaviour would lead to a considerable reduction in computation load. If neither a simpler model or a simpler noise modelling is possible, the control systems need to be designed to handle the high computational demand.

5.7 Conclusions

In this chapter, the use of a moving horizon estimator and model predictive control on a BOF converter has been studied. The estimator performance was tested by estimating the parameter values for the oxygen utilisation and bottom stirring efficiency, in the presence of disturbances on parameter values and initialisation values by using a noise corrupted simulator. With an initial offset in oxygen utilisation, the estimator quickly found the correct value. For the cases with slow variations in parameter values, the estimator produced good estimates and in combination with the controller achieved the desired carbon content in the steel. Independent disturbances with high variations led to inconsistent parameter estimates and deviations from the set-point. By adding more measurements for the estimator, the performance improved. The conclusions from this are that for high variations between batches the estimator does not have enough information from the end-point measurements to provide good estimates for the next batch.

Today, the BOF process is in general controlled by static charge calculations and the operator's experience. In this work, the use of an NMPC to find the optimal oxygen blowing time is studied. The controller uses a predefined heat recipe for the oxygen blowing rate, lance height and additions. The controller was found to perform well for the cases with accurate estimates. For the cases with significant variations, the poor estimates led to considerable deviations from the set-point. For initialisation errors, the estimator is able to compensate for initialisation errors in the carbon content by estimating the oxygen utilisation. However, by only estimating the parameter values, the estimated converter temperature differs from the real value.

The computational load of using an MHE approach for estimation is considerable. For the most complex cases, the control system is far slower than the sampling rate.

Chapter 6

Overall Conclusions and Further Work

6.1 Conclusions

In this thesis, a comprehensive model of the BOF process is further developed from a preliminary project. This model includes modelling of the off-gas system, continuous lining temperature and emulsion height, in addition to reaction kinetics between oxygen, metal and slag. The model has been validated against measurements given by SSAB, Raahe. Furthermore, the implementation of moving horizon estimator and nonlinear model predictive control is investigated. With the harsh and extreme environment of the BOF process, there are few measurements available. The fume temperature is continuously measured, and the steel and slag content is measured after the batch is finished. By using a moving horizon approach to estimate the process' state, the estimator can utilise the delayed measurements of metal- and slag analysis. Combining the estimator with an NMPC, the operator can achieve a more efficient and accurate production.

The primary foci of the modelling were to develop a model which correlated with the measurements given by SSAB and proposed process behaviour in literature. In addition, different phosphorus equilibria were evaluated, continuous lining temperature and a model for the emulsion height were implemented. The model results matched well with the measurements given by SSAB in terms of steel and slag content at the end of the blow. For some batches, the model deviated from the measurements. Further investigation showed that this could be a consequence of the loss of bottom stirring in the converter. The iron oxide content during oxygen blowing is considerably lower than expected, and the fume temperature profile does not match well with the measured temperature profile. Without more measurements during the process, it is hard to identify the possible problems.

For the phosphorus equilibria investigated, two partition ratios were found to give the best fit. Partition ratio number 4 and 13 correlated well with the process data and characteristics proposed in literature. The lining's temperature and the height of the emulsion layer matched well with the expectations.

The estimator performance was tested by using a noise corrupted process simulator. The goal of the estimator was to predict the correct parameter values in the presence of disturbances on parameter values and initialisation. For slow variations in parameter values the estimator was able to produce reasonable estimates, and in combination with the controller achieved the desired carbon content in the steel. With independent disturbances with high variations, the estimator produced inconsistent parameter values and substantial deviations from the set-point. By adding more measurements for the estimator, the performance improved. The conclusions from this are that for high variations from batch to batch, the estimator does not have enough information from the end-point measurements to provide reasonable estimates for the next batch.
The controller was configured to find the optimal oxygen blowing time and used a pre-defined heat recipe for blowing rate, lance height and additions. The controller performed well for the cases with slow variations. For large variations, the poor estimates led to significant deviations from the set-point. With initialisation errors the estimator is able to estimate the parameter values to compensate for the difference in initial carbon content, and the controller achieves the desired end-point content.
For the more complex test cases, the computational load was considerable, and the computation time was far slower than the sampling rate.

6.2 Further Work

The model's behaviour deviates from the measurements and expected behaviour in terms of the off-gas temperature and slag composition. To increase the validity of the model, the model should be further tested against batches with more measurements. Running test heats at the plant with measurements during oxygen blowing by using a sub-lance would provide much-needed information about the slag and metal composition during the heat. This would also indicate whether the assumptions in the modelling of reaction rates and the equilibriums are accurate. By adding simple instrumentation in the process such as measurements of the fume flow or the power delivered to the fan would facilitate better validation of the off-gas modelling. Improving the accuracy of the waste gas measurements would provide the estimator with more measurements, and improving the accuracy of the estimates.

The online estimation should be tested against real process data to study the end-point accuracy for batches with real disturbances. In addition, by further developing the NMPC with additions of additives and scrap, the controller can improve the accuracy regarding both carbon content and metal temperature.

For implementation in a real process, the computation time needs to be decreased. To reduce the computational load, the complexity of the model should be revised.

Bibliography

Basu, S. and Seetharaman, S. (2007), 'Studies on Dephosphorisation During Steelmaking', *Materials Science and Engineering* **Ph.D.**

Brämming, M. (2010), *Avoiding Slopping in Top-Blown BOS Vessels*.

Deo, B. and Boom, R. (1993), *Fundamentals of steelmaking metallurgy*, Prentice Hall International.

Dogan, N., Brooks, G. A. and Rhamdhani, M. A. (2009), 'Kinetics of Flux Dissolution in Oxygen Steelmaking', *ISIJ INternation* **49**(10), 1474–1482.

Dogan, N., Brooks, G. A. and Rhamdhani, M. A. (2011*a*), 'Comprehensive Model of Oxygen Steelmaking Part 1: Model Development and Validation', *ISIJ International* **51**(7), 1086–1092.

Dogan, N., Brooks, G. A. and Rhamdhani, M. A. (2011*b*), 'Comprehensive Model of Oxygen Steelmaking Part 2: Application of Bloated Droplet Theory for Decarburization in Emulsion Zone', *ISIJ International* **51**(7), 1093–1101.

Dogan, N., Brooks, G. A. and Rhamdhani, M. A. (2011*c*), 'Comprehensive Model of Oxygen Steelmaking Part 3 : Decarburization in Impact Zone', *ISIJ International* **51**(7), 1102–1109.

Drain, P., Monaghan, B. J., Zhang, G., Longbottom, R. and Murgas, I. (2016), Development of a new phosphorus partition relation for Australian steelmakers, Technical report, Melbourne.

Dyrdal, B. M. (2017), Mathematical Modelling and Simulation of Basic Oxygen Furnace, Technical report, NTNU.

Egeland, O. and Gravdahl, J. T. (2002), *Modeling and Simulation for Automatic Control*, Marine Cybernetics.

Foss, B. and Heirung, T. A. N. (2016), *Merging Optimization and Control*.

Hammervold, A. (2010), Mathematical modeling of the Linz-Donawitz converter, Technical report, NTNU.

Hammervold, A. (2011), *Model based estimation and control of a BOS converter (MSc thesis)*.

Han, M., Li, Y. and Cao, Z. (2014), 'Hybrid intelligent control of BOF oxygen volume and coolant addition', *Neurocomputing* **123**, 415–423.

Han, M. and Liu, C. (2014), 'Endpoint prediction model for basic oxygen furnace steel-making based on membrane algorithm evolving extreme learning machine', *Applied Soft Computing* **19**, 430–437.

Johansen, T. A. (2011), Introduction to Nonlinear Model Predictive Control and Moving Horizon Estimation, *in* 'Selected Topics on Constrained and Nonlinear Control', chapter 5, pp. 187–233.

Jung, S. M. and Fruehan, R. J. (2000), 'Foaming characteristics of BOF slags', *ISIJ International* **40**(4), 348–355.

Kruskopf, A. and Visuri, V.-V. (2017), 'A Gibbs Energy Minimization Approach for Modeling of Chemical Reactions in a Basic Oxygen Furnace', *Metallurgical and Materials Transactions B* **48**(6), 3281–3300.

Li, J. and Provatas, N. (2008), 'Kinetics of scrap melting in liquid steel: Multipiece scrap melting', *Metallurgical and Materials Transactions B: Process Metallurgy and Materials Processing Science* .

Mazumdar, D. and Evans, J. W. (2010), *Modeling of steelmaking processes*, CRC Press.

Naito, K., Kitamura, S. and Ogawa, Y. (2002), 'Effects of BOF top blowing and bottom stirring conditions on suppressing excessive oxidation', *Ironmaking & Steelmaking* **29**(3), 208–213.

Nocedal, J. and Wright, S. J. (2006), *Numerical optimization*, Springer.

Ohta, H. and Suito, H. (1998), 'Activities of SiO2 and Al2O3 and activity coefficients of FetO and MnO in CaO-SiO2-Al2O3-MgO slags', *Metallurgical and Materials Transactions B* **29**(1), 119–129.

Qin, S. J. and Badgwell, T. A. (2003), 'An overview of industrial model predictive control technology', *Control Engineering Practice* **11**(7), 733–764.

Rao, C. V., Rawlings, J. B. and Lee, J. H. (2001), 'Constrained linear state estimation—a moving horizon approach', *Automatica* **37**(10), 1619–1628.

Rao, C. V., Rawlings, J. B. and Mayne, D. Q. (2003), 'Constrained state estimation for nonlinear discrete-time systems: Stability and moving horizon approximations', *IEEE Transactions on Automatic Control* **48**(2), 246–258.

Rawlings, J. B. and Mayne, D. Q. (2009), *Model predictive control : theory and design*, Nob Hill Pub.

Roine, A. and al., E. (2007), 'HSC Chemistry'.

Sarkar, R., Gupta, P., Basu, S. and Ballal, N. B. (2015*a*), 'Dynamic Modeling of LD Converter Steelmaking: Reaction Modeling Using Gibbs' Free Energy Minimization', *Metallurgical and Materials Transactions B* **46**(2), 961–976.

Sarkar, R., Gupta, P., Basu, S. and Ballal, N. B. (2015*b*), 'Dynamic Modeling of LD Converter Steelmaking: Reaction Modeling Using Gibbs' Free Energy Minimization', *Metallurgical and Materials Transactions B* **46**(2), 961–976.

Seetharaman, S., McLean, A., Guthrie, R. I. L. and Sridhar, S. (2014), *Treatise on process metallurgy*, Elsevier.

Shamsuddin, M. (2016), *Physical Chemistry of Metallurgical Processes*, John Wiley & Sons, Inc, Hoboken, NJ.

Subagyo, Brooks, G. a., Coley, K. S. and Irons, G. a. (2003), 'Generation of Droplets in Slag-Metal Emulsions through Top Gas Blowing', *ISIJ International* **43**(7), 983–989.

Turkdogan, E. (2000), 'Assessment of P2O5 Activity Coefficients in Molten Slags', *ISIJ International* **40**(10), 964–70.

Turkdogan, E. T. (2010), *Fundamentals of steelmaking*, Institute of Materials(Great Britain).

World Steel Organisation (n.d.), 'About steel'.
URL: *https://www.worldsteel.org/media-centre/about-steel.html*

Zhang, Y. and Fruehan, R. J. (1995), 'Effect of carbonaceous particles on slag foaming', *Metallurgical and Materials Transactions B* **26**(4), 813–819.

Appendix A

Model Results

This appendix contains the model results that are not presented in Section 4.9. Figure A.1 presents the center reaction rates. Figure A.2 and A.3 presents the reaction rates for the different phosphorus equilibria presented in Table 4.1 and 4.2, and the partition ratios for the reaction rates presented in Section 4.9.2.

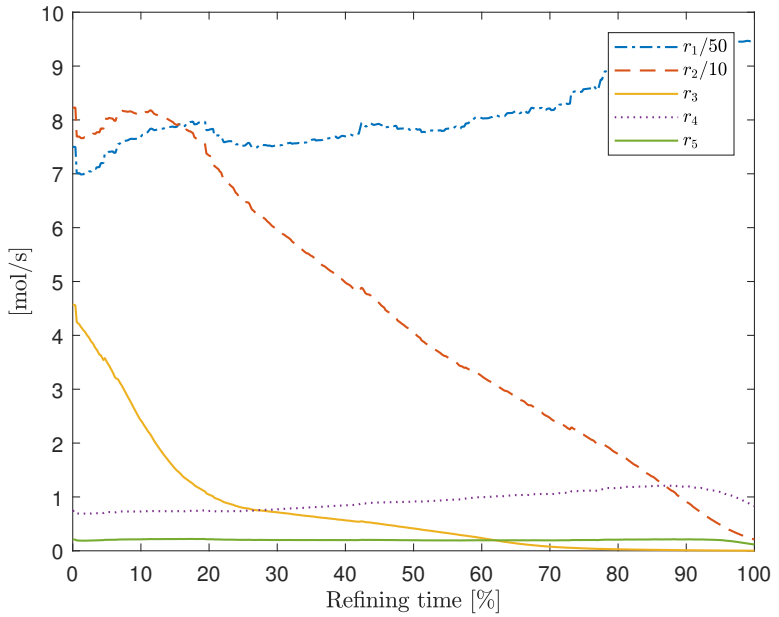

Figure A.1: Centre reaction rates

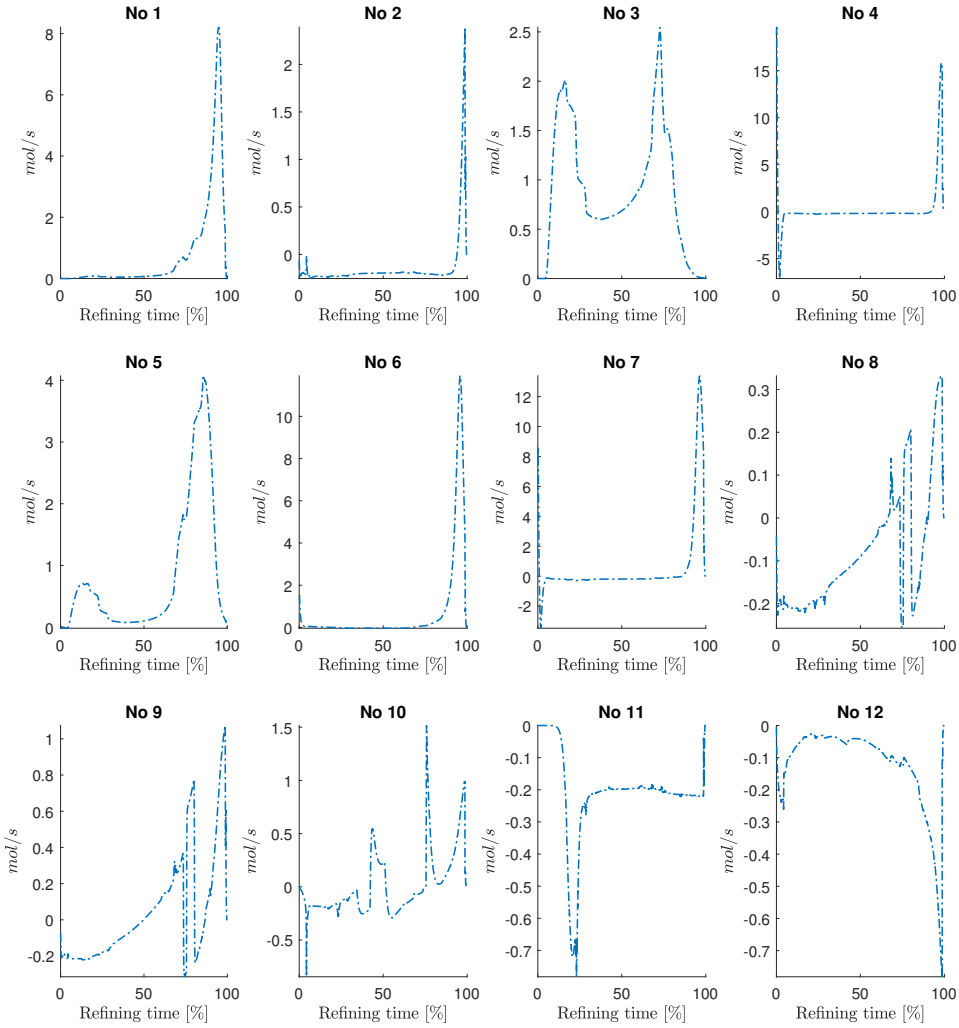

Figure A.2: Reaction rates for the different equilibriums, Table 4.1 and 4.2

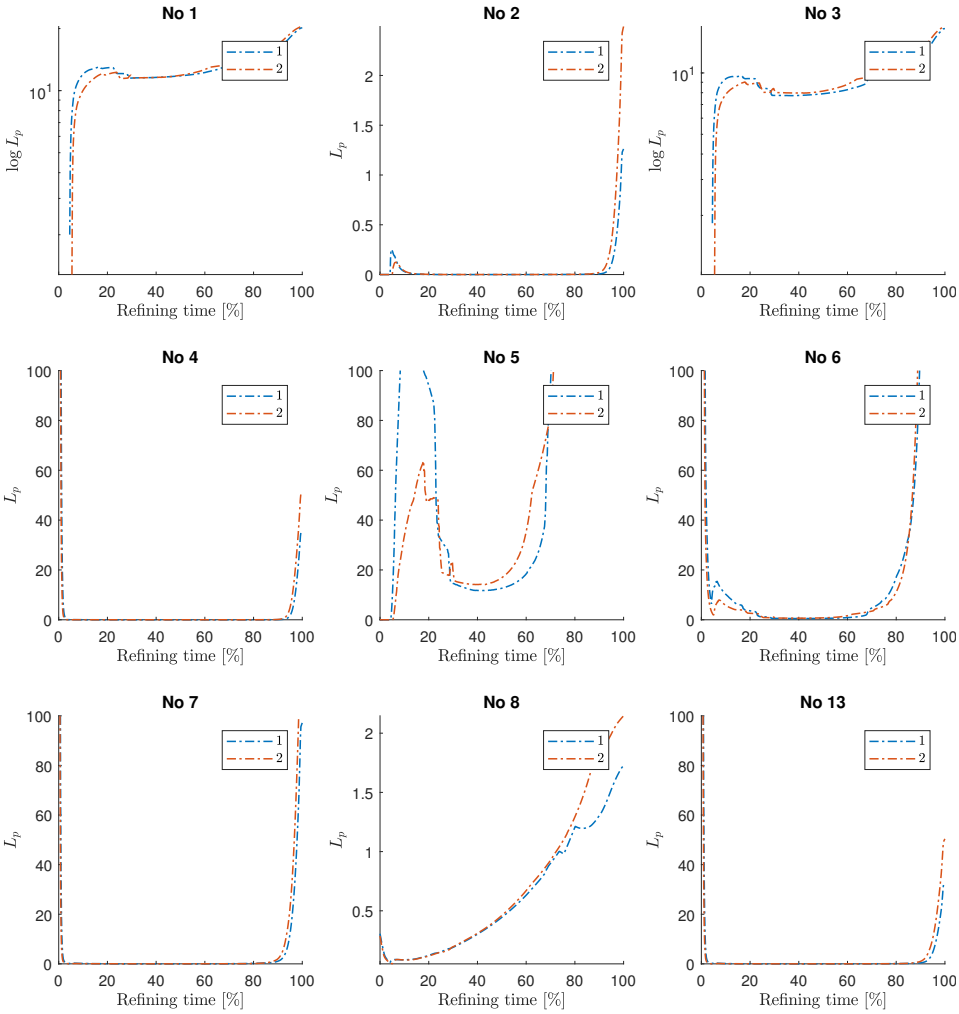

Figure A.3: Selected partition ratios for two batches